Effects of Increasing Layer Thickness in the Laser Powder Bed Fusion of Inconel 718

by

Dhiraj Amar Patil

A Thesis Presented in Partial Fulfillment
of the Requirements for the Degree
Master of Science

Approved November 2019 by the
Graduate Supervisory Committee:

Dhruv Bhate, Chair
Bruno Azeredo
Qiong Nian

ARIZONA STATE UNIVERSITY

December 2019

ABSTRACT

With the advancement of the Additive Manufacturing technology in the fields of metals, a lot of interest has developed in Laser Powder Bed (LPBF) for the Aerospace and Automotive industries. With primary challenges like high cost and time associated with this process reducing the build time is a critical component. Being a layer by layer process increasing layer thickness causes a decrease in manufacturing time. In this study, effects of the change in layer thickness in the Laser Powder Bed Fusion of Inconel 718 were evaluated. The effects were investigated for 30, 60 and 80 µm layer thicknesses and were evaluated for Relative Density, Surface Roughness and Mechanical properties, for as-printed specimens not subjected to any heat treatment. The process was optimized to print dense pasts by varying three parameters: power, velocity and hatch distance. Significant change in some properties like true Ultimate Tensile Testing (UTS), %Necking and Yield Stress was observed.

ACKNOWLEDGMENTS

Funding for this project was received from Honeywell Aerospace. I would like to thank Donald Godfrey, Engineering Fellow at Honeywell Aerospace, for his continued interest and support of the project. I would also like to thank my colleagues Cameron Noe, Paul Paradise and Mandar Shinde for helping me direct this study. I would like to thank Austin Suder and Daniel Bruce for helping me with data collection in time sensitive situations. Lastly, I would like to thank Dr. Dhruv Bhate for his support and guidance throughout the research and my Masters program.

TABLE OF CONTENTS

Page

LIST OF TABLES

Table Page

LIST OF FIGURES

Figure Page

Figure Page

Figure Page

Figure Page

CHAPTER 1

INTRODUCTION

Additive Manufacturing (AM) is a significant disruption in manufacturing of the 20th century. The ability to manufacture complex geometries has opened new opportunities for designers, manufacturers and engineers. A key challenge to the wider adoption of AM however, is the cost of producing parts, in particular when they are intended for high volumes. While analyzing the cost drivers for product life cycle managements of AM, listed some pros and cons associated with the process (Lindemann, Jahnke, Moi, & Koch, 2012). These pros and cons are listed in Figure 1, with the significant debits of AM being high machine and operating costs, and larger build times. While comparing the costs of traditional manufacturing to AM, build time can be a main driver of cost, and therefore leading a decision not to select AM processes.

Pros	Cons
- More flexible development - Freedom of design and construction - Integration of functions - Less assembly - No production tools necessary - Less spare parts in stock - Less complexity in business because of less parts to manage - No tools for productions need to hold in stock (only digital/CAD data) - Less time-to-market for products - Faster deployment of changes - Offer of individual products	- Available software is a limiting factor - High machine and material costs - High calibration effort - Quality of parts is in need of improvement - Rework of parts is often necessary (support structures) - Building time depends on the height of the part in the building chamber

Figure 1: Pros and Cons in Product Life Cycle Management of Additive Manufacturing (Lindemann et al., 201c2)

There are several different cost drivers of AM (Lindemann et al., 2012). One of the cost drivers being the manufacturing process itself, an attempt to optimize this process can be made. Several time reduction techniques such as printing with multiple lasers and

optimizing the process parameters may be explored. Increasing the number of parts per build can decrease the print time, and that increasing the part height increases the print time (Rickenbacher, Spierings, & Wegener, 2013).

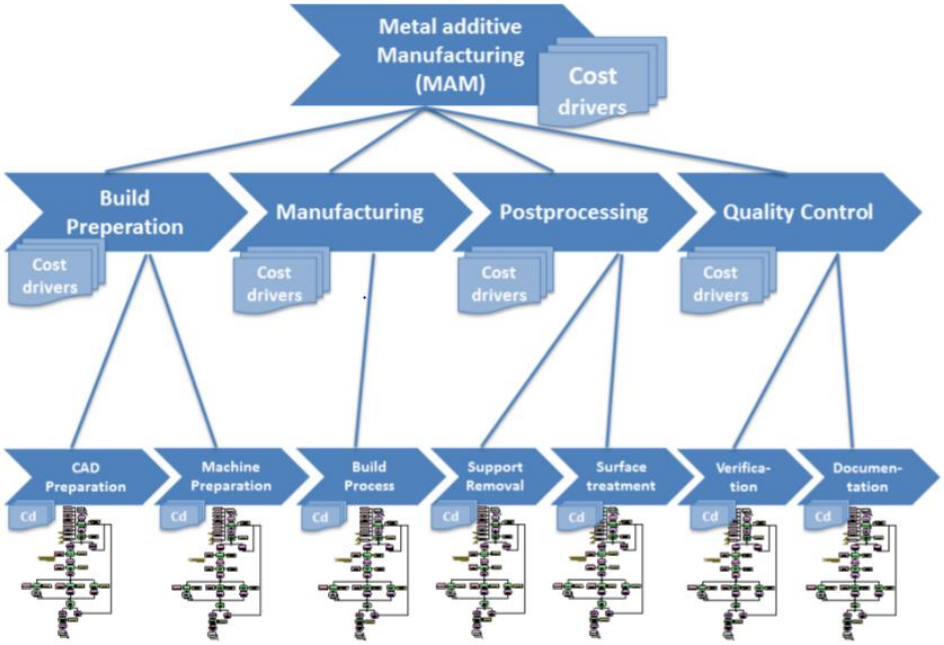

Figure 2: Cost Drivers of Additive Manufacturing (Lindemann et al., 2012)

The common factor in these two findings is that as the number of slices increase, the print time increases. In other words, increasing the layer thickness can result in decreasing the total number of slices or layers. This can be a driver of reducing the total build time and thereby driving down cost.

However, increasing the layer thickness can negatively affect properties of the manufactured parts. (Brown et al., 2018) while investigating the effects of process parameters in Laser Powder Bed Fusion (LPBF), the leading metal AM process, reviewed some effects showed by researchers of the change in parameters. For increase in layer thickness, it is observed that density decreases (porosity increases), ultimate tensile

strength (UTS) decreases and hardness decreases (Rickenbacher et al., 2013). These effects are summarized in Figure 3. Most of these studies did not explicitly attempt to optimize the process at different layer thicknesses, which, as will be discussed later, has been a focus of this thesis.

Researcher	LPBF System	Powder	Observed Effect
Modified parameter: Increase layer thickness ↗			
Dingal *et al.* (2008) [4]	Custom SLS	Iron (Atomet 86)	Inc porosity ↗ Dec density ↘ Dec hardness ↘
Kempen *et al.* (2011) [1]	SLM (Concept Laser M3)	18Ni-300 steel	Dec hardness ↘ Dec density ↘
Deffley (2012) [3]	DMLS (EOS M270)	IN718	Inc porosity ↗
Delgado *et al.* (2012) [5]	SLM (Concept Laser M3 Linear)	CL 20 (316L SS)	Dec hardness ↘ Dec UTS ↘
Delgado *et al.* (2012) [5]	DMLS (EOS M250)	DS H20 (SS)	Dec UTS ↘
Sun *et al.* (2013) [2]	SLM	Ti-6Al-4V	Dec density ↘

Figure 3: Summary of research of various AM systems and metal powders and the results of changing layer thickness, scan speed, hatch distance, or laser power (SLS = selective laser sintering, DMLS = direct metal laser sintering, SLM = selective laser melting, SS = stainless steel, Inc = increase, Dec = decrease, UTS = ultimate tensile strength, str = strength) (Brown et al., 2018).

With these debits in increase in layer thickness it is important to see these effects after optimizing the process parameters to overcome them.

1.1 Laser Powder bed Fusion Process and parameters

Laser Powder Bed Fusion (LPBF), also known as Direct Metal Laser Sintering (DMLS), can be defined as “use of laser sintering to make metal parts directly from metal powders without intermediate “green” or “brown” parts,” per ASTM standards (ASTM International, 2013). The system includes a laser source which generates the laser beam, which is then passed through an optical focusing unit. This laser beam is steered through a pair of Galvo mirrors passing through an optical window. This beam is then incident on

the build plate where the powder melts and solidifies into a part layer by layer (Saunders, 2017). This can be seen in the schematic in the Figure. 4 (a). the interaction of the laser and melt-pool behavior is shown in Figure 4 (b). It shows that the laser melts one layer of powder creating a melt-pool it also penetrates a few layers beneath the current layer as the laser moves the melt-pool solidifies into a weld melt. While this melting process takes place a vapor plume, also known as soot, is generated. With soot, small spatters of molten metal are seen as well. This process takes place in a closed environment and requires a shielding gas to avoid oxygen in the build chamber (Ladewig, Schlick, Fisser, Schulze, & Glatzel, 2016). Argon and Nitrogen are the most commonly used inert gases for this purpose. The shield gas is also responsible for carrying away the soot generated by the process to avoid impurities in the build specimen. This is a closed-circuit system and the flow can be controlled by varying the ventilator speed (Ladewig et al., 2016).

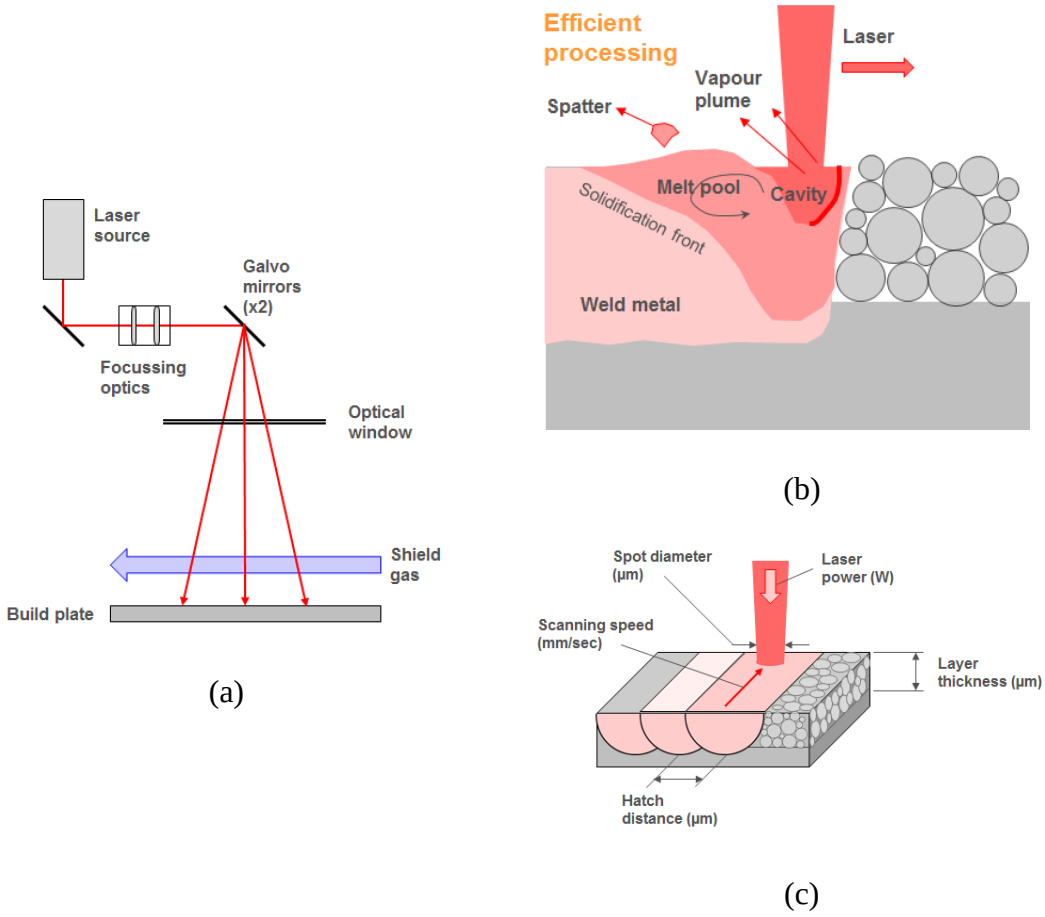

Figure 4: (a) Schematic of Laser Powder Bed Fusion process, (b) Melt Pool schematic (c) Laser Parameters. (Saunders, 2017)

The basic process parameters in the LPBF process are explained in the schematic in Figure 4 (a). A spot diameter of a laser is the diameter of the incident laser beam on the surface of the powder bed. Laser power is the incident energy of a laser per unit time. The scan velocity is the velocity at which the laser spot moves over the powder bed. Hatch distance is the distance in between two adjacent scans of the laser spot. Layer thickness is the thickness which is desired after the powder is melted (Saunders, 2017).

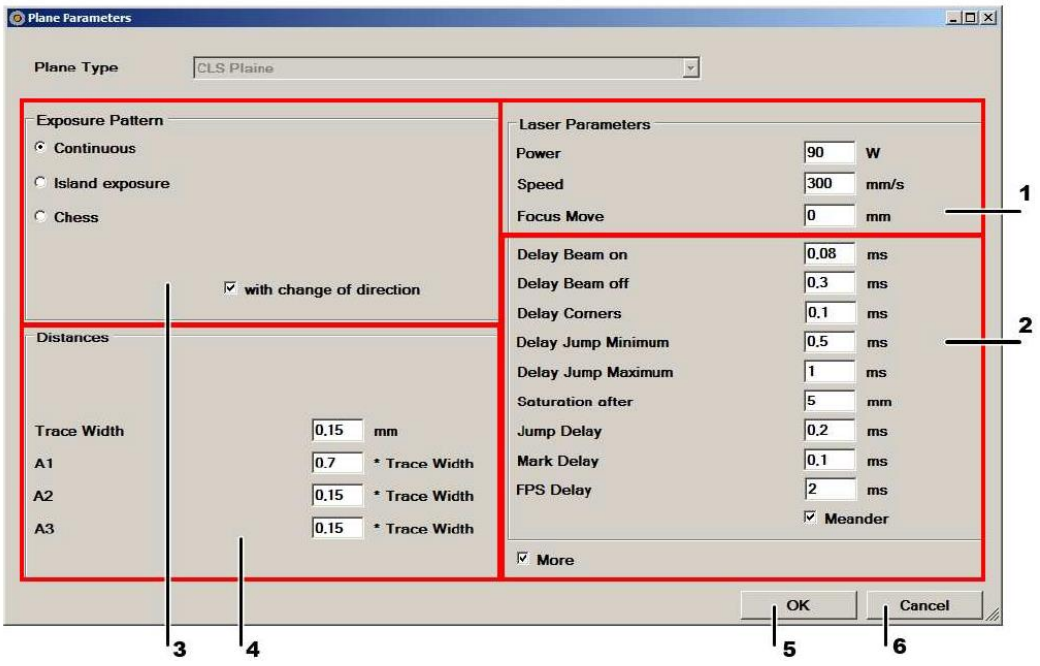

Figure 5: Laser Parameters in a Concept Laser machine, typical of an LPBF system

Inconel 718 is a well-studied alloy within the LPBF process, with several researchers having developed a set of working parameters, which are listed in Table 1.

Researcher	Equipment	Power (W)	Velocity (mm/s)	Hatch Distance (mm)	Layer Thickness (mm)
(Caiazzo, Alfieri, Corrado, & Argenio, 2017)	EOSINT M270	195	1200	0.09	0.02
(Xia et al., 2016)	SLM-150 Guangzhou	110	400	0.06	0.03
(Popovich et al., 2017)	SLM 280HL	250	700	0.12	0.05
(Sufiiarov, Borisov, & Polozov, 2014)	SLM 280HL	245	755	0.09	0.05
(Sadowski, Ladani, Brindley, & Romano, 2016)	EOSINT M 280	285	960	(not specified)	0.075
(Jia & Gu, 2014b)	(not specified)	130	400	(not specified)	(not specified)
(Tillmann et al., 2017)	SLM250HL	175	620	0.12	0.03

Researcher	Equipment	Power (W)	Velocity (mm/s)	Hatch Distance (mm)	Layer Thickness (mm)
(Wang et al., 2012)	self-developed	170	416.66	(not specified)	0.02
(Amato et al., 2012)	EOS M270	200	1200	(not specified)	0.05
(Jia & Gu, 2014a)	(not specified)	130	400	0.05	0.05
(Kuo, Horikawa, & Kakehi, 2017)	EOSINT M280	400	7000	(not specified)	(not specified)
(Alafaghani, Qattawi, & Castañón, 2018)	EOSINT M 280	400	(not specified)	(not specified)	0.04
(Jr, 2016)	EOSINT M 280	285	960	0.1	0.04
(Sochalski-Kolbus et al., 2015).	(Printed by Honeywell)	185	1200	0.1	0.02
(Karimi, Raza, Andersson, & Svensson, 2018)	Renishaw AM 250	200	(not specified)	0.1	0.075
(Choi et al., 2017)	CL Mlab	90	800	0.08	0.025

Table. 1: Laser Powder fusion with Inconel 718 literature

Parameters having all the values of power, velocity, hatch Distance and Layer Thickness were compiled and plotted on Power vs Velocity in Figure 6 and Hatch Distance in Figure 7. As can be seen, values in the literature have a wide spread across all parameters. One method of reconciling these different values is to use a term that captures the energy content of the incident beam delivered into the layer to be melted – and a metric that accomplishes this is the Volumetric Energy Density (VED). Linear Energy Density (LED) and Area Energy Density (AED) are also used in the literature, but these do not capture the contributions of layer thickness.

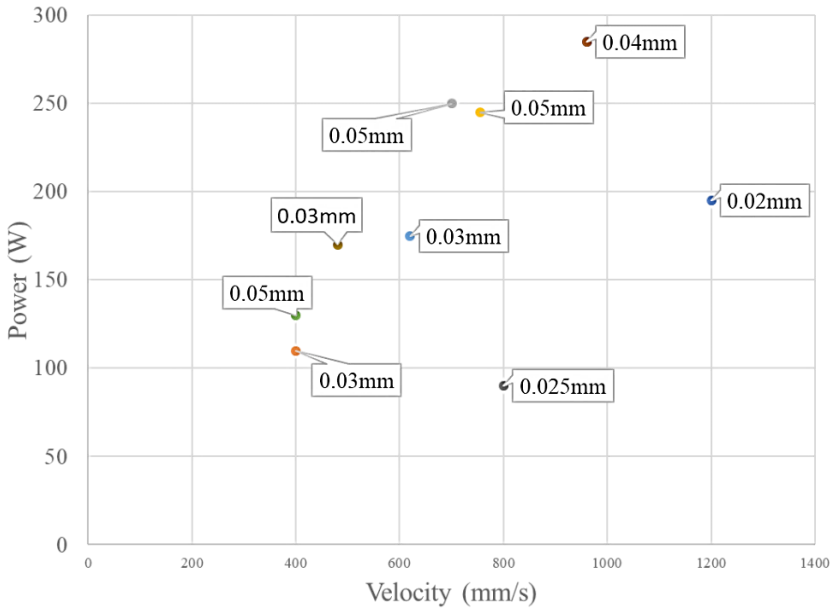

Figure 6: Power and Velocity values for Inconel 718 in literature

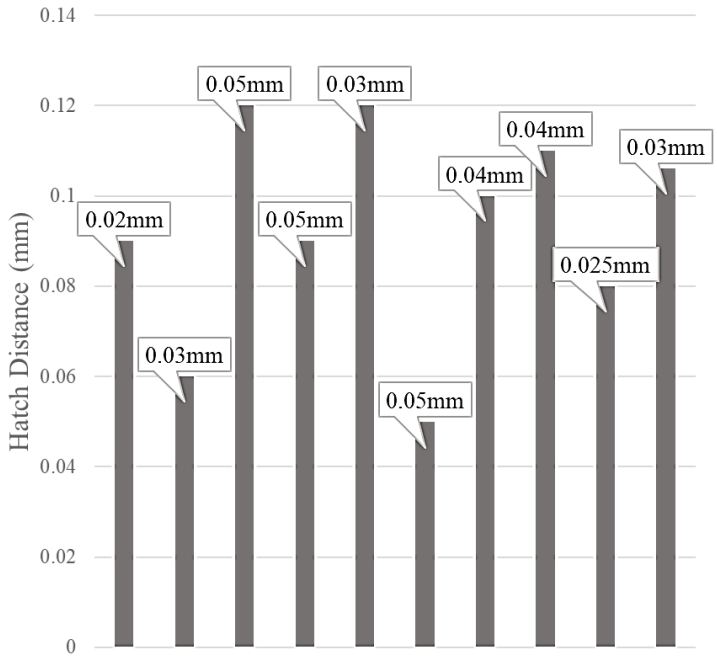

Figure 7: Hatch Distance values in literature for In 718

Values in literature which had all the parameters required for the equation are combined in Figure 8. It is found that the values in literature fall under the window of 50 J/mm^3 to 150 J/mm^3. This dataset represents a smaller number of references since not all the required values to estimate a VED were available in some papers, which are therefore excluded.

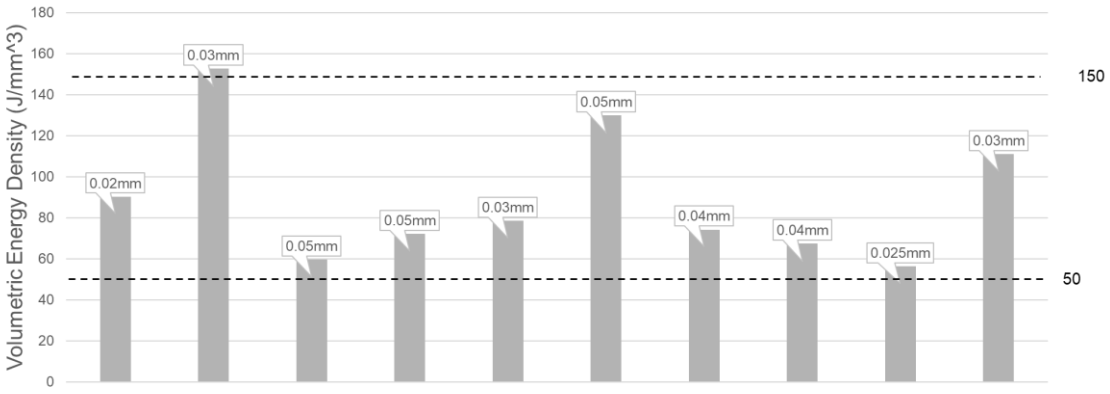

Figure 8: Volumetric Energy Density of literature values for Inconel 718

All the parameters i.e. Power, Velocity and hatch Distance can be combined in a Volumetric Energy Density (VED) which is expressed by Equation 1.

$$Volumetric\ Energy\ Density\ \left(\frac{J}{mm^3}\right) = \frac{Power(W)}{Velocity\ \left(\frac{mm}{s}\right) * Hatch\ Distance\ (mm) * Layer\ Thickness(mm)}$$

Equation 1. Volumetric Energy Density

1.2 Research Objectives

This research is motivated by the need to drive down costs in LPBF, by reducing build time. Further, this research focuses on achieving this build time reduction by increasing the layer thickness in the process, which in turn has the effect of reducing the number of layers for a given part. The following two objectives drove this research:

- The first objective of this research is to study how changes in layer thickness impact important properties in LPBF, specifically surface roughness, relative density, and mechanical behavior.
- This research also aims to assess the performance of independently optimized processes at each layer thickness, with a best-case scenario being that increasing layer thickness has no negative impact on the above mentioned properties.

The next chapter in this thesis discusses the experimental methods used in this study. This is followed by a discussion of the manufacturing of the specimens, and a chapter on the results obtained from characterizing and testing them. The thesis ends with a chapter enumerating conclusions from this work, and prescribing directions for future research.

CHAPTER 2

EXPERIMENTAL METHODS

This section describes the methods used in this study to extract data reported here. The first sub-section discusses the methodology used to design experiments, followed by sub-sections detailing the experimental methods used to make measurements.

2.1 Cliff Finding studies and Design of Experiments

For this study, a Design of Experiments (DOE) approach was used. A similar statistical approach was used for manufacturing AlSi10Mg alloy (Read, Wang, Essa, & Attallah, 2015). There are different process parameters that effect the manufacturability of parts at a particular layer thickness. The process parameters selected for this study are layer thickness, Laser Power, Laser Scan Velocity and hatch distance. Layer thickness being the main parameter of study, it was not altered, whereas other three parameters were varied to evaluate the effects.

A full factorial design with three factors and three levels was created. The three factors being Laser Power, Laser Scan Velocity and hatch spacing. Three values of each factor were selected. A high value determining the upper bound of the experiment, a low value determining the lower bound of the experiment and a medium value which is the mean of high and low value. This middle value is also called as the center point value. As the design was a full factorial design twenty-seven different parameter sets were obtained. All the parameter sets were randomized using MiniTab, a commercial statistics software. In these twenty-seven parameters each parameter had unique values of the selected three parameters.

A full factorial design with three factors and three levels was created. The three factors being laser power, laser scan velocity and hatch spacing. Three values of each factor were selected. A high value determining the upper bound of the experiment, a low value determining the lower bound of the experiment, and a medium value which is the mean of high and low value. This middle value is also called as the center point value. As the design was a full factorial design, 27 different parameter sets were obtained. All the parameter sets were randomized using MiniTab, a commercial statistics software. In these 27 parameters, each parameter had unique values of the selected three parameters.

A cliff-finding approach was taken where firstly the effective zone of printing was established. The effective zone of printing was defined as the set of parameters giving specimens free of obvious visual defects. Once an effective zone was established, a second DOE was conducted within that zone to explore the main effects and interactions, and also set the context for the selection of an optimum set of process parameters at each layer thickness.

Relative Density (%) was the main response of the experiment. After the final effective zone was established for a layer thickness, this response was recorded. The desired response was considered as a relative density of 98% and above, based on discussions with industry members.

2.2.1 30 μm Layer Thickness

Researchers use different parameters to print fully dense parts for the same material – this applies to layer thickness as well, which were each printed with different laser parameters. For selection of parameters for the baseline layer thickness in this study (30 μm), the upper bound and the lower bound of the parameters were selected with respect to the values found

in the literature. A layer thickness of 30 µm is a conservative, supplier recommended value, and as such was selected as the baseline to compare findings from thicker layers against.

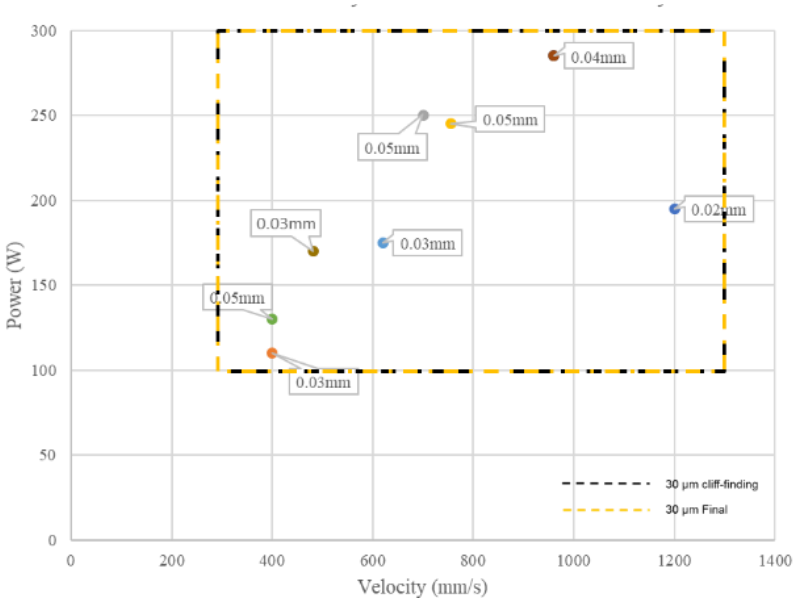

Figure 9: Pwer(W) and Velocity (mm/s) for cliff-finding and final DOE selection of 30 µm layer thickness.

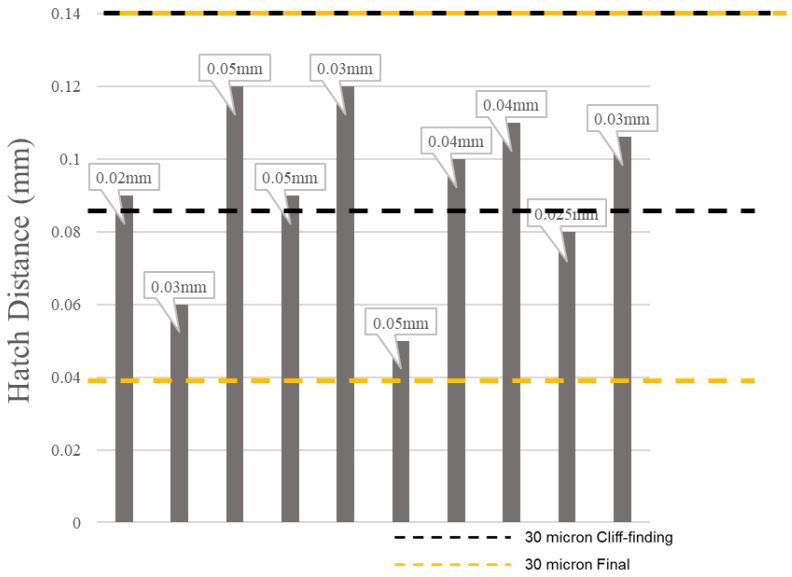

Figure 10: Hatch Distance (mm) for cliff-finding and final DOE selection of 30 µm layer thickness.

Figure 9 shows the values selected for the cliff-finding study enveloping values studied in the literature for power, velocity and hatch spacing. No unusual behavior was seen with the selected power and velocity during the cliff finding experiments. Thus, the same parameters were utilized for the final experiment. This was not the case for the hatch distance, Figure 10 shows that the values in the literature fall within the hatch distance values selected for the cliff finding experiment. For the cliff finding experiments, a hatch distance value of 0.04 mm was chosen for the lower bound, 0.09 mm as the medium value and 0.14 mm for the upper bound. Specimens with a hatch distance of 0.04 mm showed unusual surface behavior and caused a failed print. The top face of the specimen had small sphere-shaped recast material which caused coater blade and specimen contact, causing the print to fail. Similar surface behavior was seen with the parts having the hatch distance of 0.04 mm. Other specimens did not show any unusual behavior. As a result of these findings, the lower bound of the hatch distance was shifted to 0.09 mm for the final experiment. Table 2 summarizes all the values of the parameters that were changed from the cliff finding experiment to the final experiment for 30μm layer thickness.

Parameter		Low	Medium	High
Power (W)	Cliff-finding	100	200	300
	Final	100	200	300
Scan Velocity (mm/s)	Cliff-finding	300	800	1300
	Final	300	800	1300
Hatch Distance (mm)	Cliff-finding	0.04	0.09	0.14
	Final	0.09	0.115	0.14

Table 2. List of parameters used for 30 μm layer thickness design of experiments

2.2.2 60 μm Layer Thickness

Increasing the layer thickness directly drives an increase of material to be melted, thus it is evident that optimum parameters will differ from that of the baseline. As discussed previously, one method of reconciling parameters at varying layer thicknesses is to use the Volumetric Energy Density (VED) expression. An assumption may be made that the energy concentration required for melting the powder should remain constant, even as layer thickness changes.

Having established a working window of laser parameters for 30μm layer thickness, this dataset was leveraged to define the cliff-finding parameters for the 60μm layer thickness. As shown in Figure 11, the VED values for 30μm were plotted for the 27 data points that were studied. Using the same laser parameters, but changing layer thickness to 60μm results in a curve with lower VED values. This curve was then adjusted by modifying laser parameters to match the VED for 30μm parameters, for initial cliff-finding experiment. While not strictly a statistically robust method, this approach has the benefit of limiting the range of parameter exploration needed.

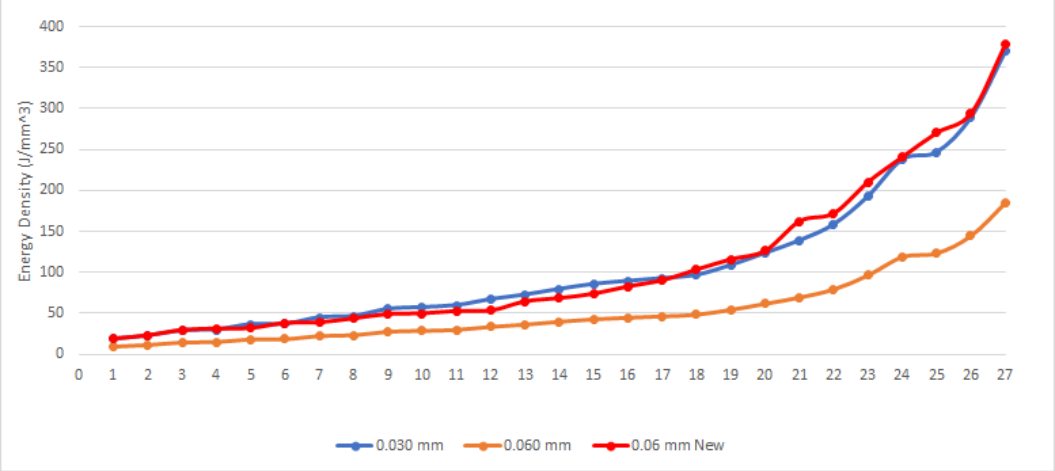

Figure 11: Comparison and adjustment between Volumetric Energy Density for cliff-finding experiment of layer thickness 30 µm and 60 µm

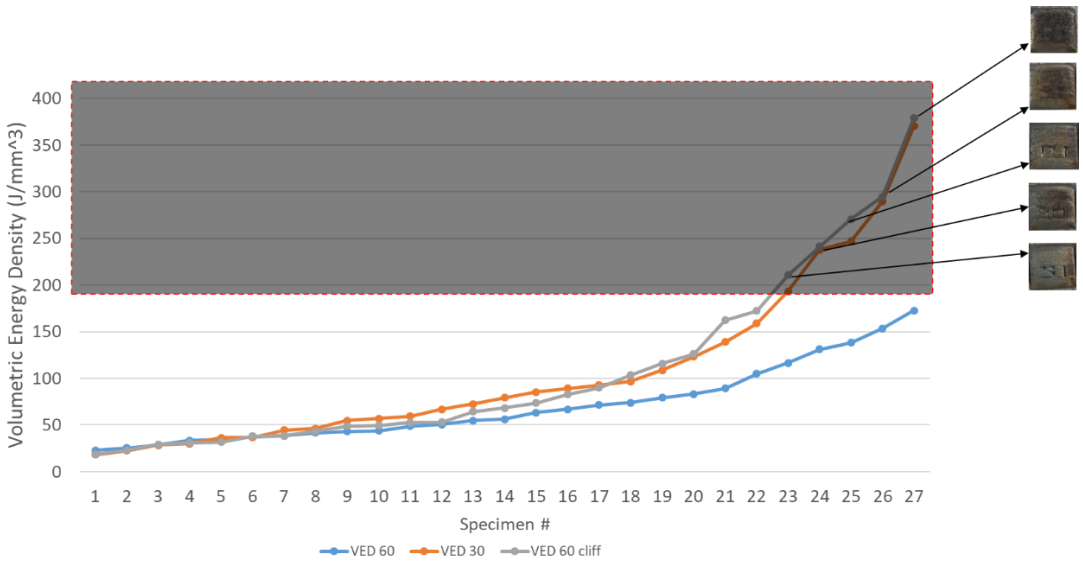

Figure 12: Comparison and adjustment between Volumetric Energy Density for cliff-finding and final experiment of layer thickness 60 µm

After printing the 60 µm cliff finding specimens, it was seen that the specimens with VED higher than 200 J/mm^3 had discoloration and lost fidelity, as shown in Figure 12. These specimens also generated significant soot and discoloration of specimens, both attributable to high VED. To avoid this phenomenon, parameters were further adjusted to

limit maximum VED below 200 J/mm^3. This experiment suggests that VED, as calculated using the method previously described, does not completely address the physics of melting due to increases in layer thickness.

To achieve lower VEDs for the 60 µm studies, laser power was decreased to 290 W for the upper bound, and velocity range was decreased to 350 - 1100 mm/s for the lower and upper bound, respectively. Figure 13 shows the Power and velocity change in parameter window for the cliff finding experiment and final DOE. The operating process margin has reduced with increase in layer thickness. Figure 14 shows the reduction in margin in the hatch distance as well. The hatch distances were narrowed down to 0.08 and 0.1 mm for lower and upper bound. With these adjusted VED values, final DOE specimens for 60 µm were printed.

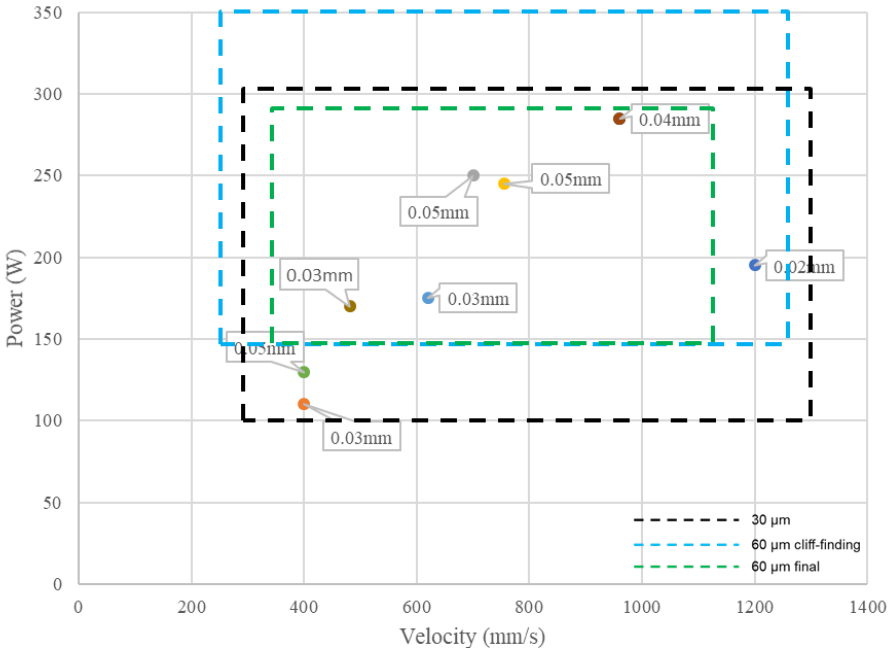

Figure 13: Power(W) and Velocity (mm/s) for cliff-finding and final DOE selection of 60 µm layer thickness.

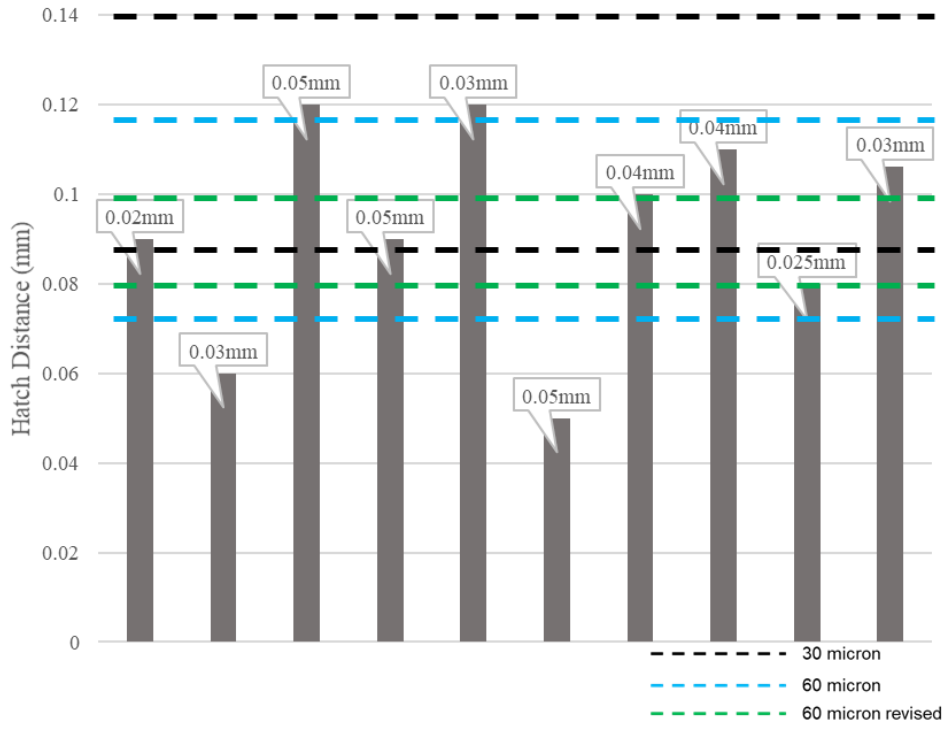

Figure 14: Hatch Distance (mm) for cliff-finding and final DOE selection of 60 µm layer thickness.

Table 3 summarizes all the values of the parameters that were changed from the cliff finding experiment to the final experiment for 60 µm layer thickness.

Parameter		**Low**	**Medium**	**High**
Power (W)	Cliff-finding	150	250	350
	Final	150	220	290
Scan Velocity (mm/s)	Cliff-finding	220	720	1220
	Final	350	725	1100
Hatch Distance (mm)	Cliff-finding	0.07	0.09	0.11
	Final	0.08	0.09	0.10

Table 3. List of parameters used for 60 µm layer thickness design of experiments

1.1.3 80 μm Layer Thickness

A similar approach was taken for increasing the layer thickness further to 80 μm. The VED for the 60 and 80 μm layer thicknesses were compared by changing the layer thickness but keeping the parameters the same, as shown in Figure 15. Similar to 60 μm layer thickness, a decrease in the VED was seen as the layer thickness was increased to 80 μm. To overcome this VED gap, parameters from the 60 μm final DOE were adjusted to match the VED of that layer thickness. Keeping the same value for velocity, values for hatch distance and power were changed. Hatch distance was reduced to 0.07 mm for the lower bound and was increased to 0.11 mm for the upper bound. Power was increased to 250 W for upper bound, and 350 W for the lower bound. With these adjusted parameters, the cliff finding experiment was printed.

After printing the cliff finding experiment, it was found that similar to the 60 μm cliff finding experiment, specimens with VED greater than 105 J/mm^3 had discoloration, as shown in Figure 16. The VED value for discoloration dropped from 200 J/mm^3 for 60 μm to 105 J/mm^3 for 80 μm. To avoid these specimens with poor fidelity, the values of the parameters were adjusted to lower the VED for the final experiment for 80 μm. Figure 16 shows the adjusted VED plots for specimens for cliff-finding and for final DOE for 80 μm layer thickness.

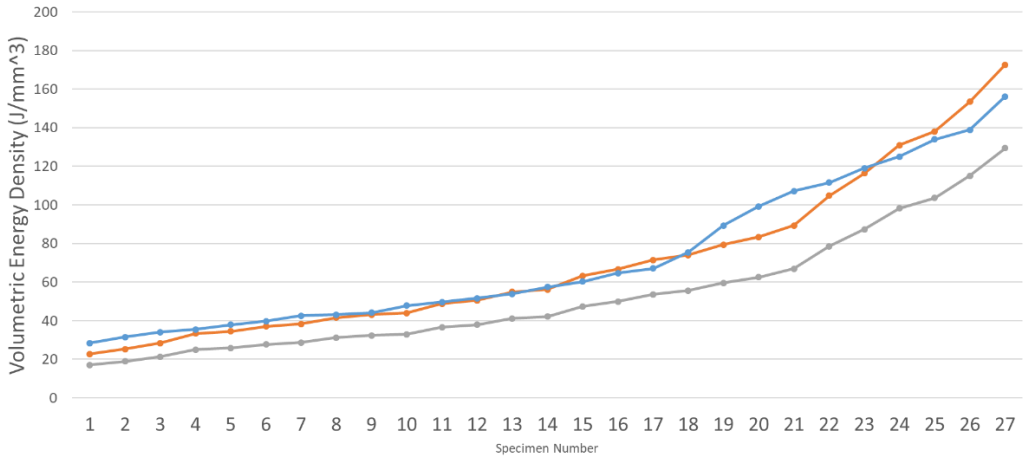

Figure 15: Comparison and adjustment between Volumetric Energy Density for cliff-finding experiment of layer thickness 60µm and 80µm

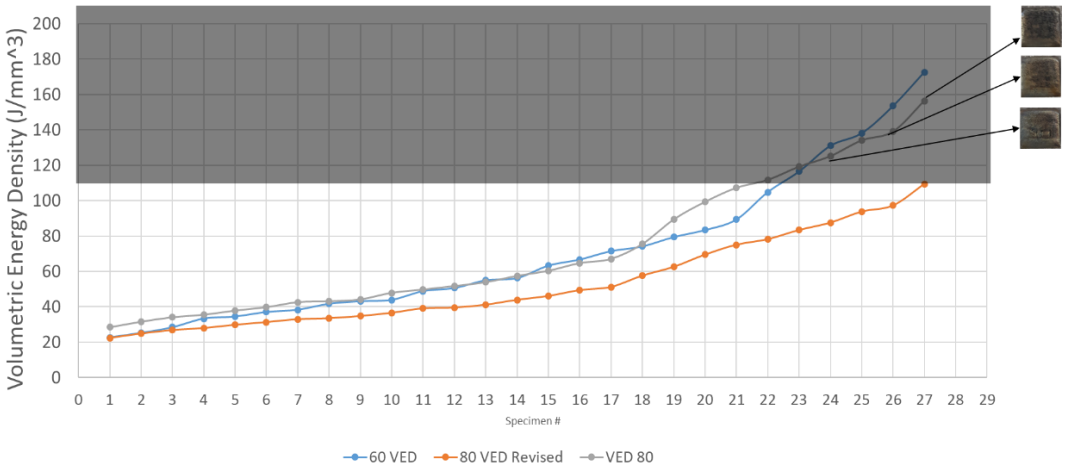

Figure 16: Comparison and adjustment between Volumetric Energy Density for cliff-finding and final experiment of layer thickness 80 µm

For this adjustment of decreasing the VED for 80 µm layer thickness experiment, keeping the values of power the same, velocity was increased to 500 mm/s for the lower bound and 1400 mm/s for the upper bound. Hatch distance was increased to 0.08 mm for the upper bound and was decreased to 0.1 mm for the upper bound. These parameters were used to print the final experiment for 80 µm layer thickness.

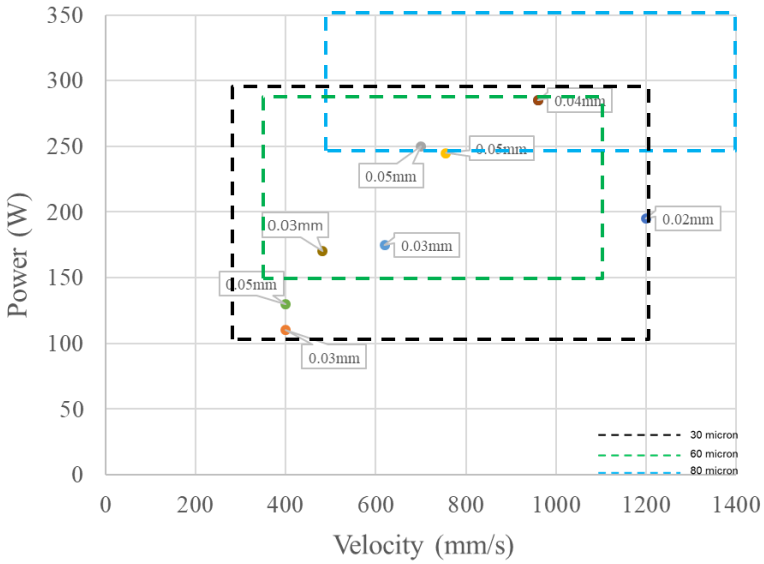

Figure17: Power(W) and Velocity (mm/s) for cliff-finding and final DOE selection of 80 µm layer thickness.

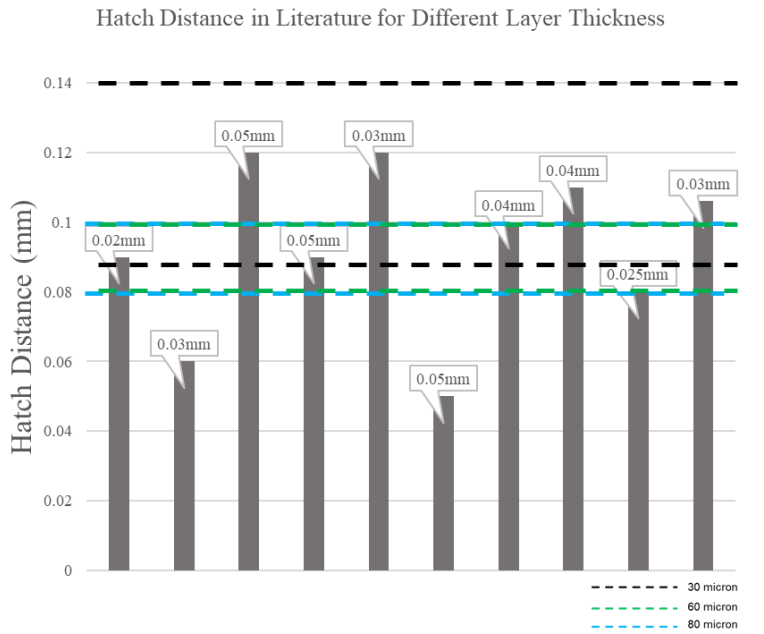

Figure 18: Hatch Distance (mm) for cliff-finding and final DOE selection of 80 µm layer thickness.

Table 4 summarizes all the values of the parameters that were changed from the cliff finding experiment to the final experiment for 80 μm layer thickness.

Parameter		**Low**	**Medium**	**High**
Power (W)	Cliff-finding	250	300	350
	Final	250	300	350
Scan Velocity (mm/s)	Cliff-finding	350	725	1100
	Final	500	950	1400
Hatch Distance (mm)	Cliff-finding	0.07	0.09	0.11
	Final	0.08	0.09	0.10

Table 4. List of parameters used for 80 μm layer thickness design of experiments

2.2 Method for Relative Density Measurements

For this study, the Archimedes method of density measurement was used to measure density of all the specimens manufactured for this study. An *A&D HR 250A* Density Measurement Kit and balance was used to measure the weights in air and water. Figure 19 shows the schematic of the density measurement kit that is placed inside the balance measurement unit used for measurements in air and water

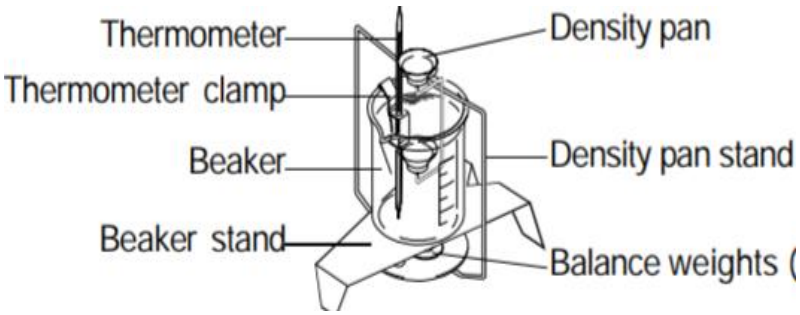

Figure 19: Density measurement kit

The procedure for the Archimedes method used in this study is as follows: Temperature of water, and time, was recorded at the beginning and during the test. Weight of the specimen in air was recorded after waiting for 30 seconds for the value to stabilize. Weight in air was recorded three times to get replications. After recording the weight in air, the specimen was immersed in distilled water and surface air bubbles were removed with a wire brush. This specimen was then placed in the density pan immersed in water. A 30 second wait time was provided to allow the balance to stabilize. This weight in water was measured three times by removing the specimen and re-immersing. The balance was tared (reset to zero) each time before placing the specimen on the pan.

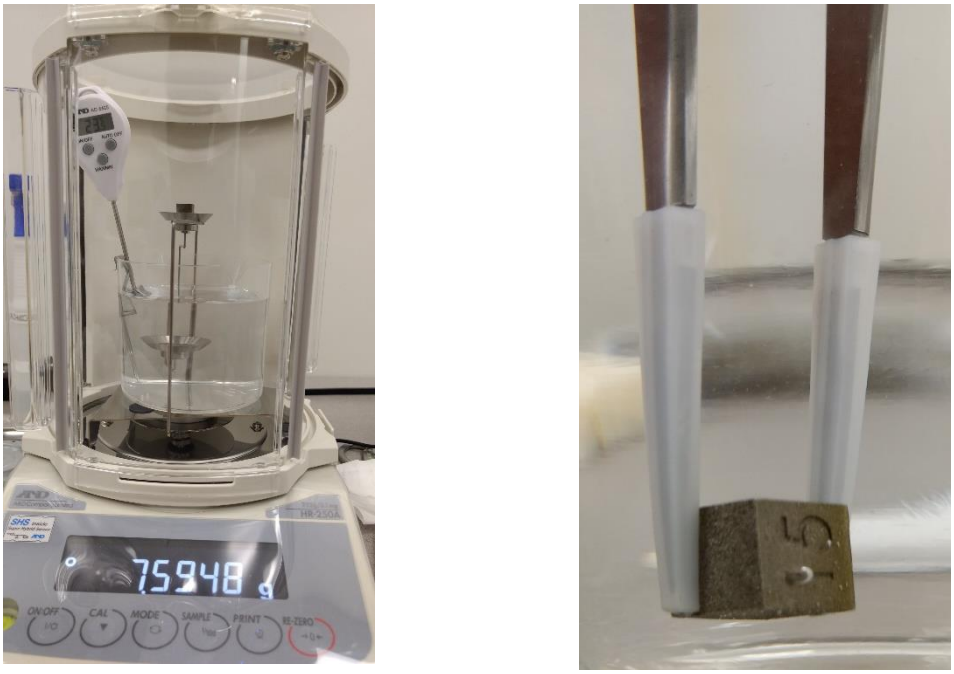

(a) (b)

Figure 20: (a)Balance and density measurement kit (b) Surface air bubble

After the weight of water was recorded, the following formula was used to calculate the specific gravity of the specimen.

$$\rho = \frac{A}{|B|} * (\rho_O - d) + d$$

Equation 2: Equation used to calculate Density of a solid

Where ρ is the density of sample (g/cm^3), A is the weight in air (g), B is the weight in water (g), ρ_0 is the density of water, d is the density of air (g/cm^3). Density of air was assumed to be 0.0012 g/cm^3, per a standard density chart shown in Figure 21.

°C	ρ=/kg m^{-3}									
	0.0	0.1	0.2	0.3	0.4	0.5	0.6	0.7	0.8	0.9
21	997.9948	9731	9513	9294	9073	8852	8630	8406	8182	7957
22	997.7730	7503	7275	7045	6815	6584	6351	6118	5883	5648
23	997.5412	5174	4936	4697	4456	4215	3973	3730	3485	3240
24	997.2994	2747	2499	2250	2000	1749	1497	1244	0990	0735
25	997.0480	0223	9965[B]	9707[B]	9447[B]	9186[B]	8925[B]	8663[B]	8399[B]	8135[B]

[A]Obtained from *CRC Handbook of Chemistry and Physics*, 78th edition, 1997-1998.
[B]The leading figure decreases by 1.

Figure 21: standard densities of water

Distilled water was used to measure the weight in liquid. Table 4 was used calculate density of distilled water for temperature at the time of recording the values. The values were converted to the relevant units before performing the calculations. After calculating the relative density of the sample three times for each measurement reading, mean of the three values was taken as the final relative density of that sample

2.2 Interferometry for surface roughness

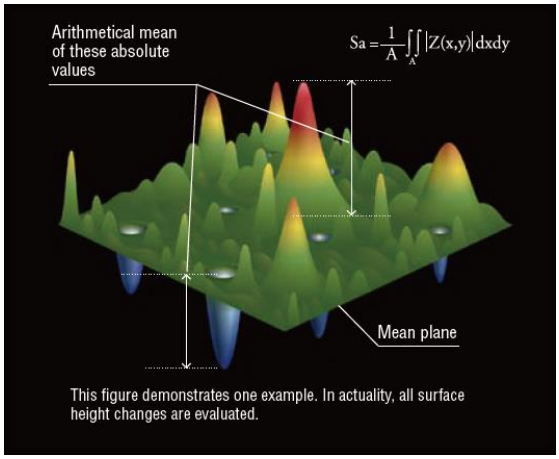

(a)

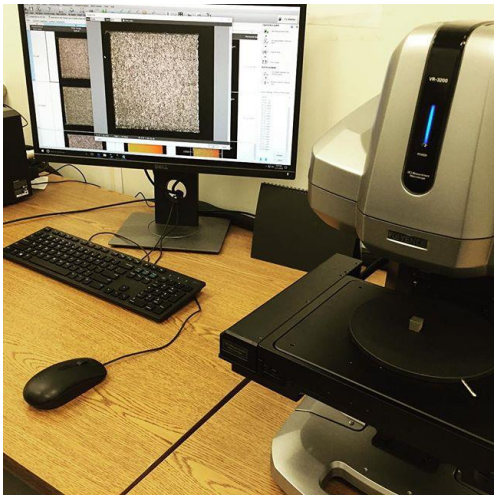

(b)

(c)

Figure 22: (a) S_a illustration (b) Equipment setup for Surface roughness measurement (c) Keyence VR-3000 structured white light 3D scanning microscope

Surface roughness was measured on a Keyence VR-3000 structured white light scanning microscope. For this study, surface roughness was measured over an area of the specimen denoted by S_a in mm. Sa is similar to the more commonly used R_a, where R_a is arithmetical mean height of a line corresponding to the profile of the surface along that

line. S_a is not measured over a line, but over an area, as shown in Figure 22 a. It provides an absolute value of mean surface roughness by calculating the difference of the height of a peak and valleys from the arithmetical mean plane of the surface. Visualizer, the compatible software with the equipment was used to calculate and report the S_a of all samples.

2.4 Mechanical Testing

An Instron 5985, a 250kN load capacity universal testing machine was used to perform tensile tests. All the tests were conducted at a strain rate of 10^{-3}, following ASTM E8. The tensile specimen cross-section thickness was measured using a micrometer screw gauge prior to testing. This thickness was used to calculate the stress in the specimen. A non-contact video extensometer was used for strain measurements. For the extensometer to recognize the deformation, two white spots were marked in the gauge section of the specimen. The extensometer was calibrated, and load cell and displacement were set to zero, each time a new specimen was loaded on the machine.

Figure 23: Instron 5985

Data from the machine was then analyzed to compute modulus, yield stress, true Ultimate Tensile Strength (UTS, percentage elongation, and percentage necking.

CHAPTER 3

MANUFACTURING

Two different types of specimens were fabricated for this study. The first category of specimens was designed and manufactured to execute the DOE for the cliff-finding and final parameter selections discussed previously. The second set of specimens were used for mechanical testing. Specific details associated with the manufacturing process for each of these specimen types are discussed in turn below.

2.1 DOE Specimens

As described earlier, for developing the process parameters for higher layer thickness, a DOE approach was implemented. These DOEs had 27 different combination of three parameters (power, velocity, hatch distance).

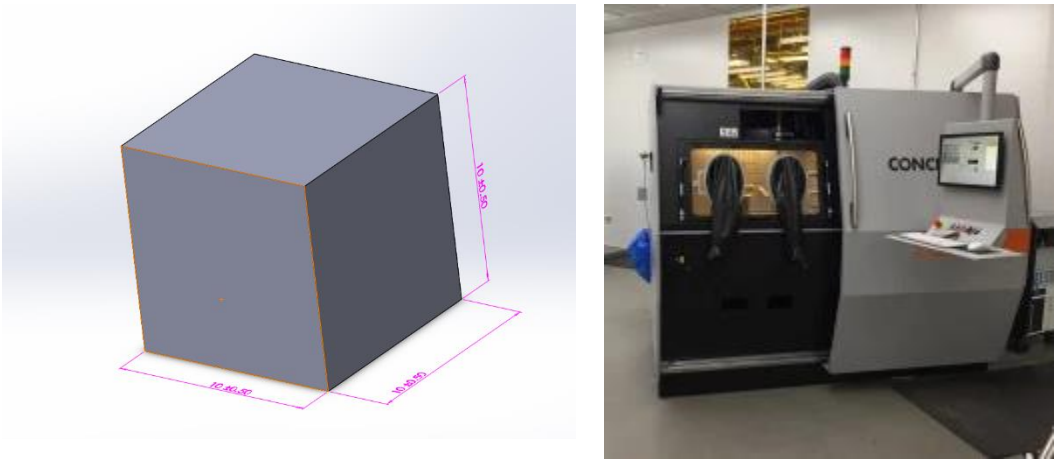

(a) (b)

Figure 24: (a) DOE Specimen (b) Concept Laser M2

Figure 24 (a) shows the 10 mm cube designed for these experiments, which is a design commonly used in the literature. Figure 18b shows the Concept Laser M2, a leading commercial Laser Powder Bed Fusion (LPBF) metal Additive Manufacturing machine. This machine has a single fiber laser with maximum power of 400 W and a spot size of 0.05mm. The build envelope is 250 x 250 x 350 mm^3. Inconel 718, obtained in powder form from Praxair Inc., was the material used to manufacture all the specimens in this study. Argon was used as a shielding gas. The ventilator speed was set to 60%, and dosage of the powder was set to 300%, both standard supplier-recommended settings.

Materialise Magics, a machine compatible slicing software was used for build preparation. The cubes were arranged in a grid of 5 x 5. The cubes were rotated to a 45^o from the x axis to minimize the coater blade interaction with the geometry. A scan angle of 45^o alternating its direction every layer was used for all the specimens. All cubes had a single contour and its laser parameters were set to match the parameters of the raster, which in turn were specific to the laser parameter settings specific to each specimen. To capture any variance due to the build location the same set of twenty-seven cubes was replicated in four different locations of the build plate. The cubes were labeled in the software using the mass labeling tool with two numbers separated with a dot, where the first digit indicated the specimen number and the second indicated the location of the build plate. This labeling was done on the vertical face of the cube. The cubes were placed on the build plate and no support was added. The cubes were placed 5 mm apart from each other in one set of 27 specimens. These four sets were equidistantly centered.

Figure 25 (a) shows the top view of the build as setup in the Magics software. The four chosen locations on the build plate results in a wide range of build coverage across the

plate. Figure 25 (b) shows the build illustration in the machine. The parts were marked with an order relative to the direction of the ventilator to minimize re-melting of soot particles and effecting properties of other specimens. All the different parameters for printing were taken from Table 2, Table 3, Table 4. A total of six separate builds with 108 specimens on each build were printed for these DOEs.

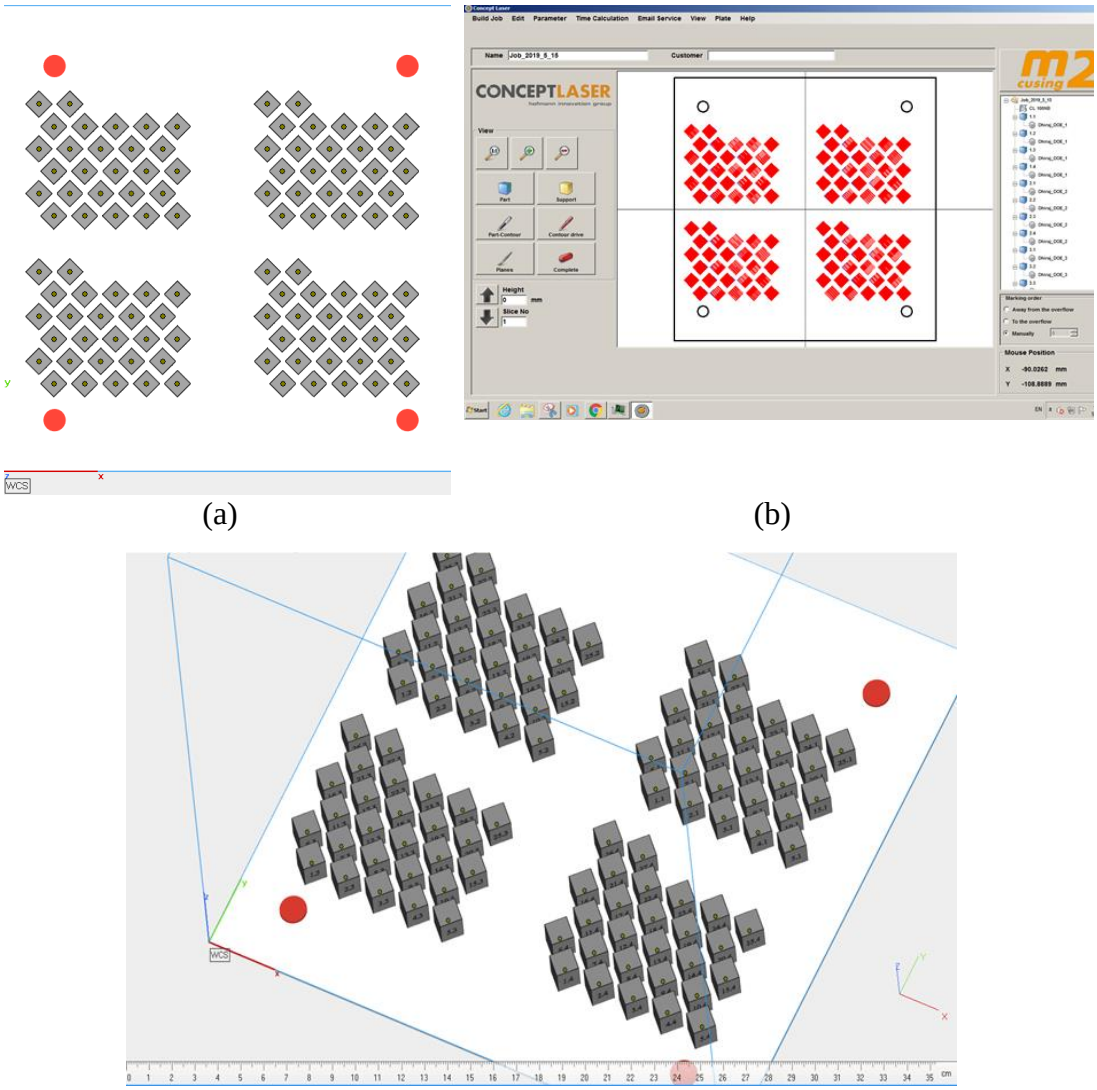

(a) (b)

(c)

Figure 25: (a) Top view of build platform (b) Build illustration on machine (c) Angled view of the build platform

Figure 26 shows the finished print with the coater blade and shield gas direction. It is evident that different parameters result in varying surface effects. The effects for one cube were similar to the cubes with same parameters in a different location. The specimens were cut off the build plate using a FANUK wire EDM machine. No further stress relief, heat treatment or post-processing was performed on these specimens. These specimens were then analyzed for relative density.

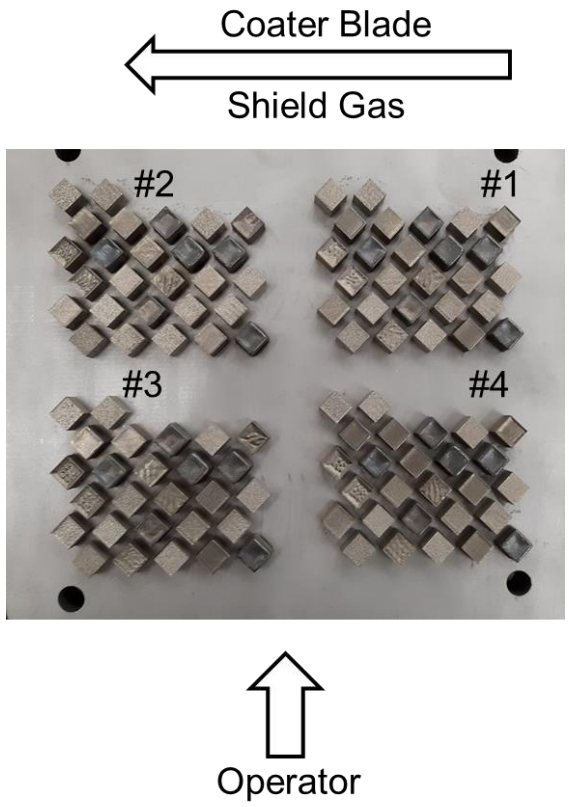

Figure 26: Finished Print with 108 specimens.

2.2 Mechanical Test Specimens

2.2.1 Specimen Design

The tensile test specimen geometry was designed based on ASTM E8 standard, which covers testing of metallic materials for yield strength, yield point elongation and tensile strength. This standard provides various geometries of specimen broadly classified as plate type and round specimens (ASTM E8, 2010). Plate type specimen, as shown in Figure 27, was selected for this study, as it is easy to characterize surface roughness on flat faces of the specimen, and also due to its ease of printing. As a primary variable in this study was layer thickness it was important to print all the samples in vertical direction – this likely represents the worst case scenario with regard to mechanical properties. The specimen height was also selected to fit within the build envelope of the Concept Laser M2.

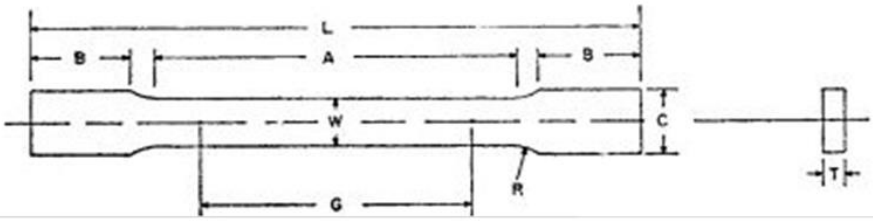

	Subsize Specimen
	6 mm [0.250 in.] Wide
	mm [in.]
G—Gage length (Note 1 and Note 2)	25.0 ± 0.1 [1.000 ± 0.003]
W—Width (Note 3 and Note 4)	6.0 ± 0.1 [0.250 ± 0.005]
T—Thickness (Note 5)	
R—Radius of fillet, min (Note 6)	6 [0.250]
L—Overall length, (Note 2, Note 7, and Note 8)	100 [4]
A—Length of reduced section, min	32 [1.25]
B—Length of grip section (Note 8)	30 [1.25]
C—Width of grip section, approximate (Note 4 and Note 9)	10 [0.375]

Figure 27: ASTM E8 Standards for plate geometry (ASTM E8, 2010)

A specimen was then designed considering all the minimum requirements of the standard and FEA analysis was carried out for the tensile testing to ensure low stress concentration factors, which in turn ensure failure within the gauge section. For a minimum fillet radius of 6mm, a high stress concentration (19%) is observed at the point of reduced cross section shown in figure 28. The stress concentration factor reduces to under 1.1 at 18mm fillet radius, which was the final value used for this study.

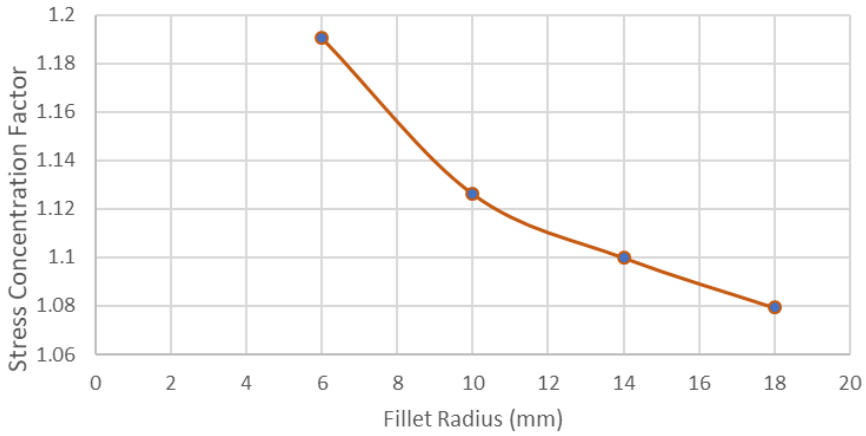

Figure 28: Stress Concentration Factor vs fillet radius

Based on all the above considerations, the final design of specimen is shown in the figure 29, Total length of specimen is 108.5 mm, it has gauge section of 25 mm, width of gauge section is 6 mm and 10 mm for the gripper section. Thickness was selected as 2 mm.

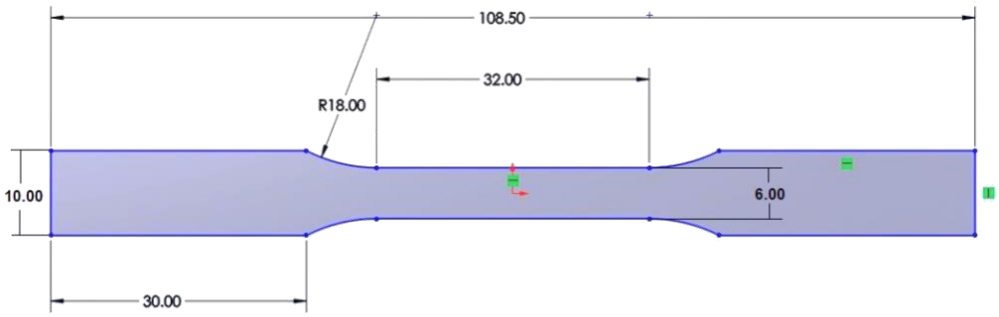

Figure 29: Final Specimen Design

2.2.2 Manufacturing of ASTM dog-bone specimen.

Whereas the DOE specimens represented a wide range of laser parameters, the mechanical test specimens were printed with the optimized parameters for each layer thickness, discussed in the next chapter. Figure 30 (a) shows a set of 100 specimens of the selected design arranged in a grid of 10x10. The location of these specimens was recorded in terms of X and Y coordinates within the build plate, to study location effects on the properties of the specimens. The specimens were oriented vertically to face the operator or perpendicular to the coater blade. This was done to minimize area of contact to prevent any possible failures due to coater blade and the specimens. The specimens were built vertically to avoid any support structure in the gauge section. Solid support of 2 mm was added to the bottom of the specimens to account for wire EDM machining.

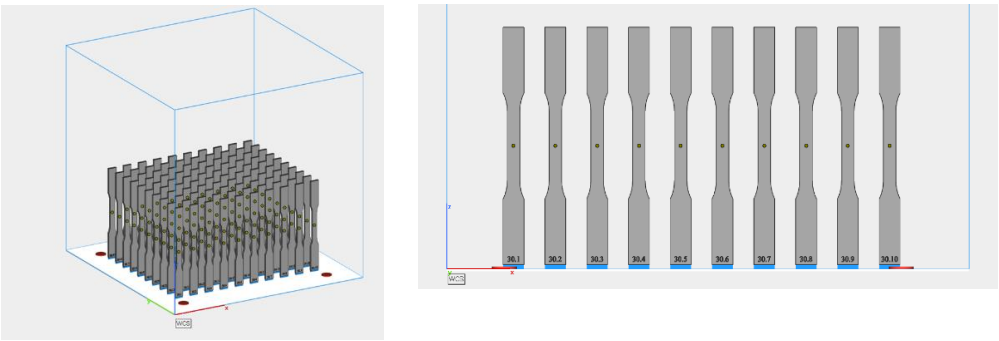

(a) (b)

Figure 30: (a) Orthogonal view of the build (b) Side view of the build

Figure 31 shows a successful print (without any machine pauses during the build, or defective specimens) for 2 mm thick vertical specimens with the optimized parameters. Similar prints were conducted all three layer thicknesses. There were no visual defects observed for any of these builds. Specimens were labeled using the mass label in Magics software to ensure traceability, using similar methods to those discussed previously. A total of 300 specimens, 100 for each of the three layer thicknesses, were obtained after wire EDM process and then were tested to get properties. Once again, these were not subjected to any heat treatment or post-processing steps prior to testing.

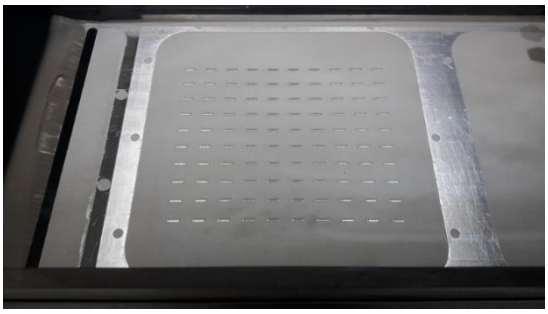

(a)

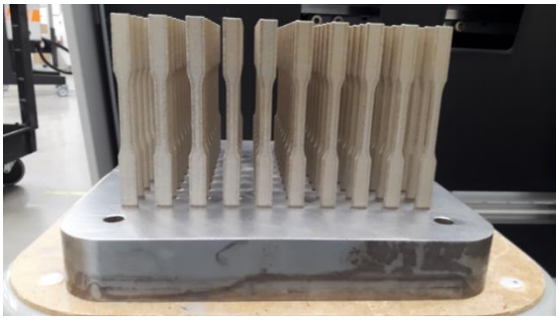

(b)

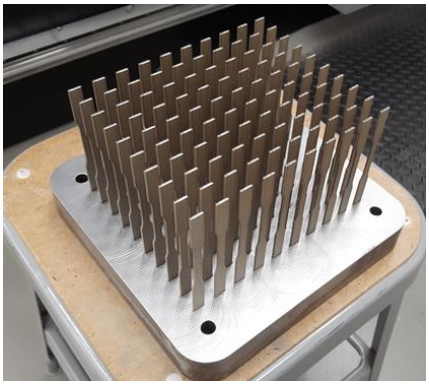

(c)

Figure 31: (a) Build chamber of a finished build (b) Vertical specimens on build plate (c) Specimens on build plate

CHAPTER 4

RESULTS

This section discusses results obtained from the different experiments conducted in this study using methods and specimens manufactured as described in previous chapters. The first section in this chapter discusses results from the DOE study conducted to estimate relative density of cube specimens at all 3 thicknesses. This is followed by sections discussing how this data correlates with Volumetric Energy Density (VED), and how this may be used to select an optimum parameter set for each thickness. Finally, these optimum values at each thickness are used to print dog-bones to extract mechanical property data, which is presented in the final section.

4.1 Relative Density Estimations

Relative density, being the response of DOE, was measured for all the cubes printed with final DOE parameters developed after the cliff finding experiments, where qualitative assessments were conducted to eliminate certain parameter sets. None of the cliff finding experiment parameters were measured for relative density. All these results are based upon the measurements taken by the Archimedes method discussed in chapter 2.2

4.1.1 Relative Density analysis of 30 μm Layer Thickness

Figure 32 shows the analysis of all 108 specimens printed with the final DOE parameters developed for 30 μm layer thickness. At 100 W, only specimens printed with velocity 300 mm/s were denser than 98%. At 200 W, it is seen that only specimens with medium velocity of 800 mm/s were high in relative density and most of the rest were below

98%. For a combination of 200 W and 1300 mm/s, a low hatch distance of 0.09 gave highly dense parts. At 300 W, a slower velocity of 300 mm/s resulted in less dense parts, whereas for medium and high velocity the relative density was high.

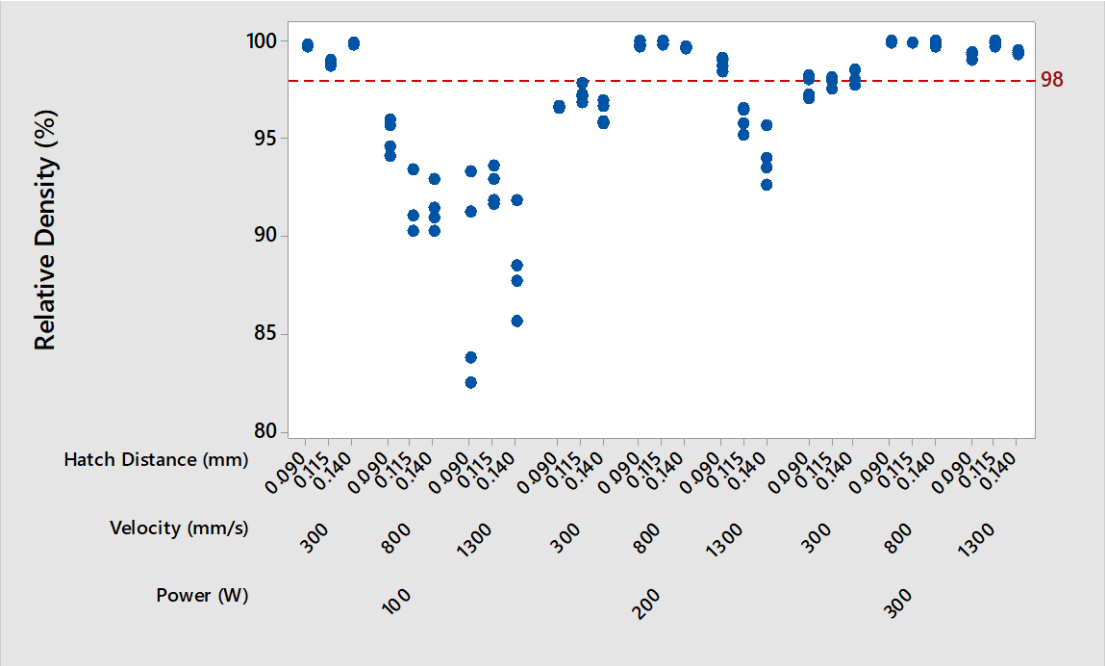

Figure 32: Individual value plot for 30 µm layer thickness

Figure 33 (a) shows a Pareto chart for the effects of parameters on the response. It can be seen that almost all parameters have a significant effect on the response, with power and velocity having the most effect. Hatch distance did not have as significant an effect on relative density. Figure 33 (b) shows the main effects plot for 30 µm layer thickness. These are the averaged values for particular value e.g. for power 100 W, all the combinations consisting of that power were averaged and the value was reported on the plot. The relative density increases as power increases and decreases for higher velocity and hatch distance.

These plots only predict the effects and trends of the parameters chosen for this study at 30 µm. This is not considered a deciding factor for selecting optimized parameters.

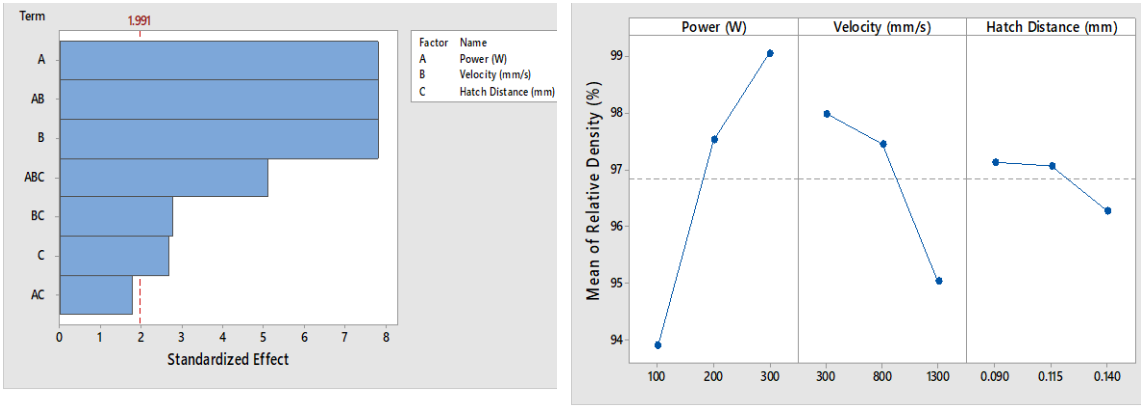

(a) (b)

Figure 33: (a) Pareto chart for 30 µm layer thickness, (b) Main effects plot for 30 µm layer thickness

Figure 34 shows a plot of relative density and volumetric energy density of 108 specimens with 30 µm layer thickness. It includes values from the literature discussed earlier. The chosen parameters for this study can be represented in a single term of VED. When VED and Relative density were plotted it is clearly seen that the values of high relative density were concentrated in margin of VED 50 to 150 J/mm^3. Specimens with VED less than 50 J/mm^3 had a significant drop in Relative density and can be because of lack of fusion defect. Whereas, the specimens on the higher side of VED above 150 J/mm^3 had a comparatively low density. It can be inferred that, for densification to occur a minimum amount of energy is required and with a higher amount of energy the porosities

can be occurring due to some phenomenon. The values from literature also fall under the same window.

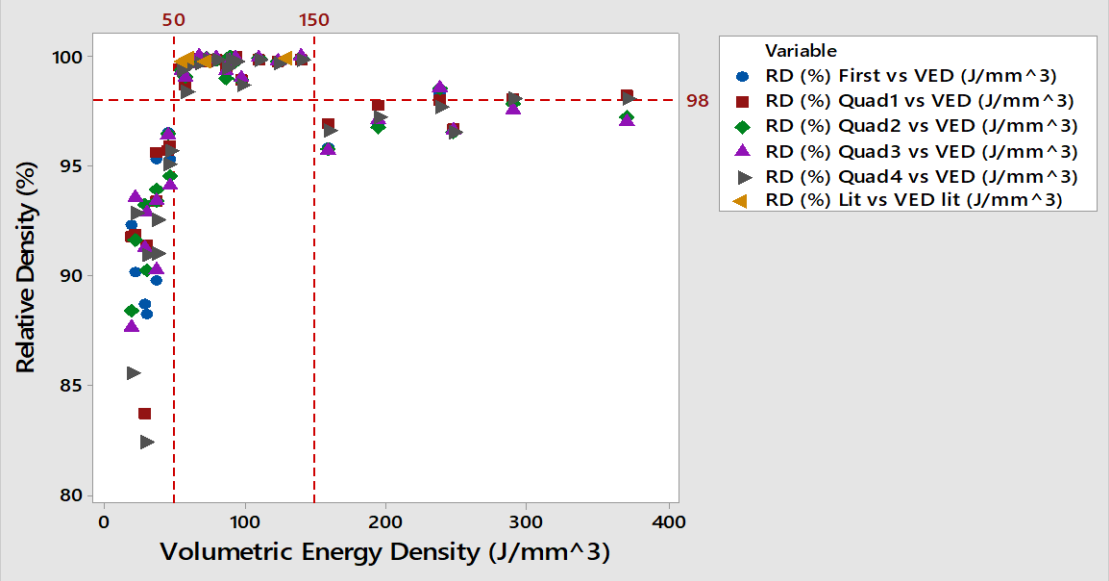

Figure 34: Plot of Relative Density vs Volumetric Energy Density for 30 µm

4.1.2 Relative Density analysis of 60 µm Layer Thickness

Similar to the results for 30µm layer thickness Figure 35 shows the individual value plot for 60µm layer thickness. In this relative density as a main response of all the parameters manufactured with 60µm layer thickness and the final DOE parameters form Table: 3 are seen. It is observed that specimens printed with low Power of 150 W show high relative density in the low and medium velocity region where as the relative density drops as velocity is increased to 1100 mm/s at this Power. As the Power is increased to 220 W the specimens are observed to have a larger relative density for medium and high velocities whereas the relative density decreases with drop in velocity to 350 mm/s. Similar to 220W increasing the Power to 290 W resulted in increase in relative density for medium and high velocity, but decreased in specimens with 350 mm/s of velocity in that region. There was no significant effect of change in hatch distance in this plot.

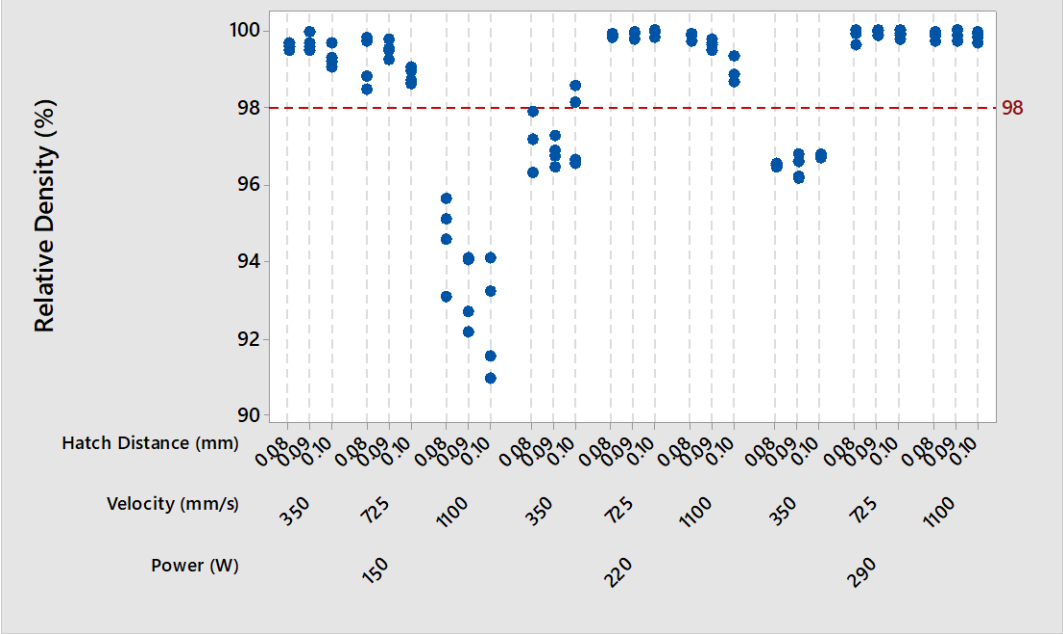

Figure 35: Individual value plot for 60µm layer thickness

Pareto chart in figure 36 (a) shows the effects of parameters on the response. It is seen that the parameter effect is similar to 30µm layer thickness data, where Power and velocity have the most significant effects whereas hatch distance did not show any significant effects on the response. These effects are seen for the parameters been selected for this study. For the Main Effects plot in figure 36 (b) where all the response for a particular parameter value are averaged. For power it is seen that the relative density increases as the power increases from 150 W to 220 W but drops a bit for 290 W. For velocity the relative density is lower with the velocity of 350 mm/s and 11000 mm/s but is higher for the medium velocity of 725 mm/s. The velocity trends are different for 60µm than they are for 30µm. The hatch distance shows a trend of decreasing relative density with increasing hatch distance from 0.08 mm to 0.1 mm. These plots give an understanding

of the process parameters selected for the study and are not used as a selection criterion for the optimal parameters.

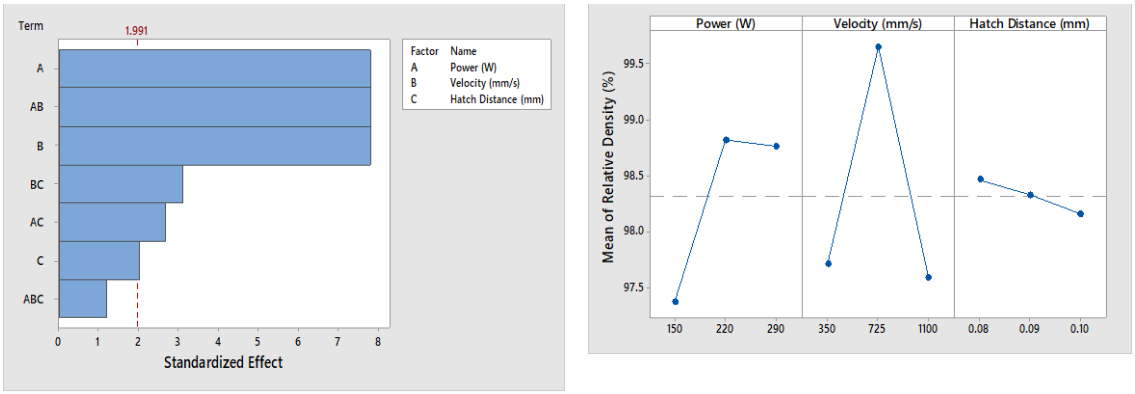

(a) (b)

Figure 36: (a) Pareto chart for 60µm layer thickness, (b) Main effects plot for 60µm layer thickness

Relative density and Volumetric Energy Density are plotted in Figure 37. It is seen that specimens with VED lower than 33 J/mm^3 and larger than 90 J/mm^3 have lower relative densities. For specimens with VED less than 33 J/mm^3 a sudden drop in the relative density was seen and surface texture were observed visually. These surface textures indicate lack of fusion. Specimens with those with VED higher than 90 J/mm^3 had discolored surfaces and was observed to be more significant than that for 30 µm layer thickness specimens.

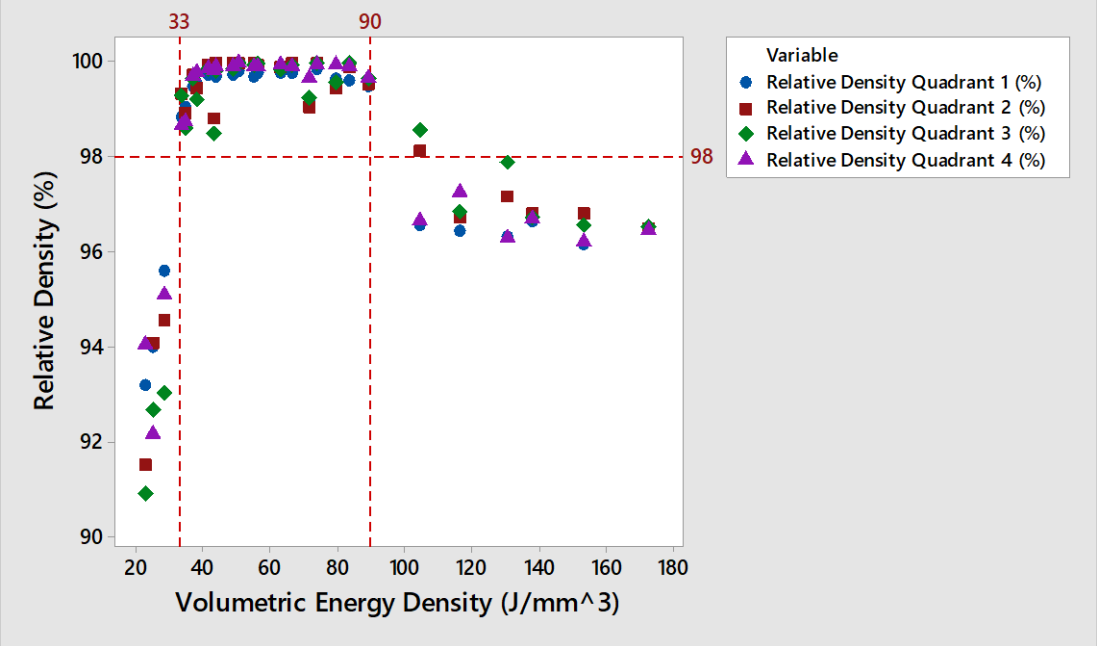

Figure 37: Plot of Relative Density vs Volumetric Energy Density for 60µm

4.1.3 Relative Density analysis of 80µm Layer Thickness

Individual value plot for 80µm layer thickness is shown in Figure 38. Relative densities were measured for the cube specimens printed with 80µm layer thickness with the use of final DOE parameters from Table 4. Results were similar to the results from 30µm and 60µm layer. Specimens printed with Power 250 W showed less relative density for high velocity of 1400 mm/s with hatch distance 0.09 mm and 0.1 but high densities for lower hatch distance of 0.08 mm. For Power 300 W all the specimens had high relative density. Similar results were observed for even more high Power of 350 W.

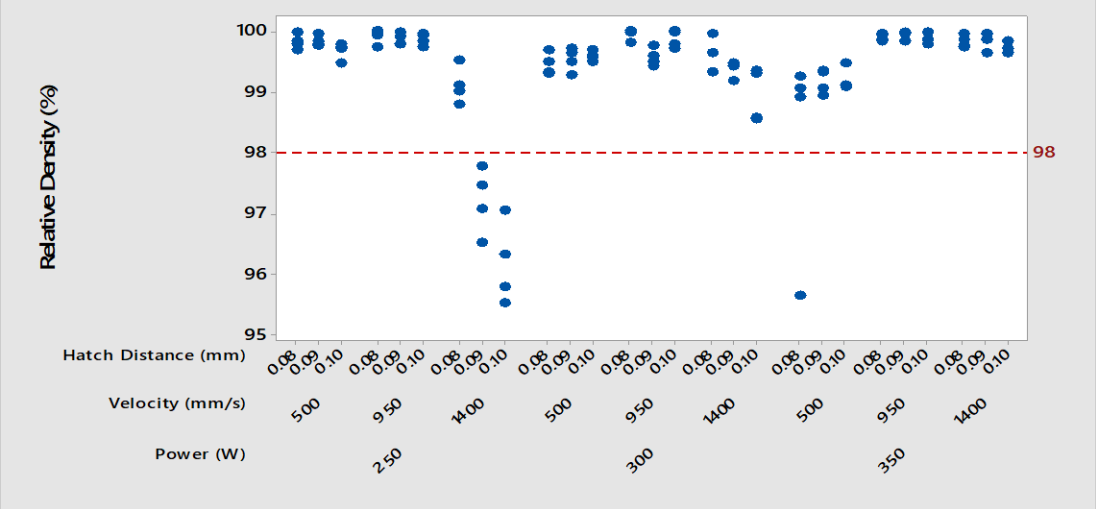

Figure 38: Individual value plot for 80µm layer thickness

Figure 39 (a) shows a pareto chart with effects of the selected parameter range to the response of DOE. It indicates that interaction between velocity and Power has the most significant effect on the relative density of a specimen. Although all the parameters had statistically significant effects, the selected range of velocity had the most effect on relative density. Whereas the selected range of hatch distance had the least effect on relative density. Figure 39 (b) shows the main effects plot for density analysis on the 80µm final DOE specimens. It is seen that the results defer from figure 33 (b) but are similar to Figure 36 (b). Relative Density increases with increase of Power from 250 W to 300 W and slightly drops for 350 W. As the velocity was increased from 500 mm/s to 950 mm/s the relative density increases but decreases as the velocity is increased further to 1400 mm/s. Hatch distance did not show any significant difference when compared to Figure: 36 (b) and 33 (b) and shows similar trend of decreasing of relative density with an increase in hatch distance. As these values are averages of all the relative density values it is not used as the criterion for selecting the final parameters.

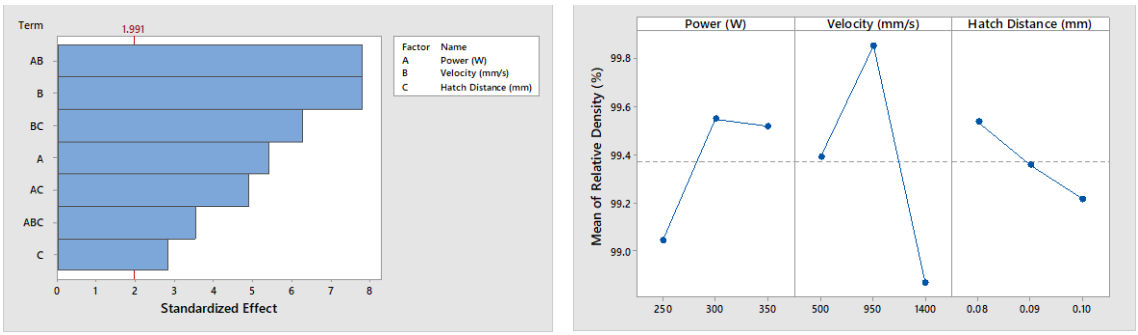

(a) (b)

Figure 39: (a) Pareto chart for 80µm layer thickness, (b) Main effects plot for 80 µm layer thickness

Figure 40 shows a plot of relative density and volumetric energy density for DOE specimens printed with 80µm layer thickness. It is observed that specimens with relative density higher than 98% lie between 25 J/mm^3 and 98 J/mm^3. Specimens with VED larger than 98 J/mm^3 had low densities for some specimens whereas all the specimens with VED smaller than 25 J/mm^3 had low densities. This is similar to the results found in Figure 34 and Figure 37. It is also observed for most of the specimens lie between the window of 25 J/mm^3 and 98 J/mm^3 where as there are less specimens outside of this window.

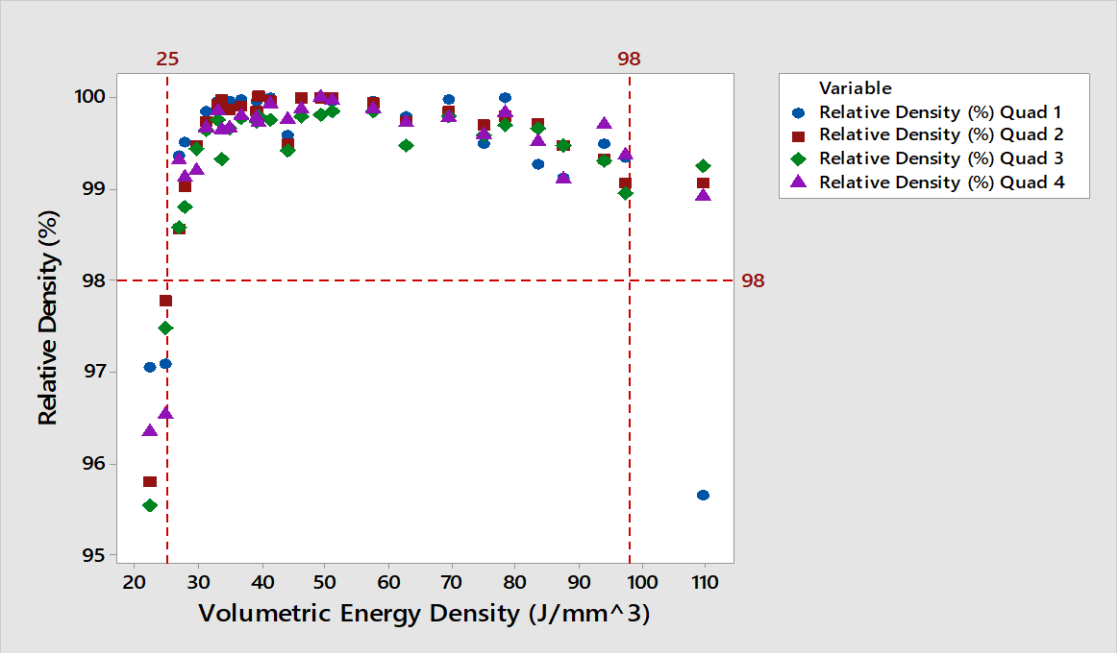

Figure 40: Plot of Relative Density vs Volumetric Energy Density for 80µm

4.2 VED and Relative Density Comparison

It has been observed that there is an optimal operating window of VED for different layer thicknesses. Specimens outside of that window have resulted in lower relative densities.

Figure 41 shows the comparison of the VED windows for 30µm, 60µm and 80µm layer thickness DOE specimens. As the values of relative densities have been recorded for 108 specimens in several locations for each layer thickness, for comparison of VED these values were averaged over the four locations. 27 averaged values of each layer thickness were compared. It is seen that VED window shrinks as the layer thickness increases. For 30µm layer thickness VED window is 50 J/mm^3 to 150 J/mm^3, for 60µm layer thickness this window shrinks to 33 J/mm^3 to 90 J/mm^3. For 80µm layer thickness it is more than that of 60µm but less than 30µm layer thickness. There is also a constant decrease observed

at the lower bound of the VED window with increase in the layer thickness. The lower bond decreasing from 50 J/mm^3 to 33 J/mm^3 and further to 25 J/mm^3.

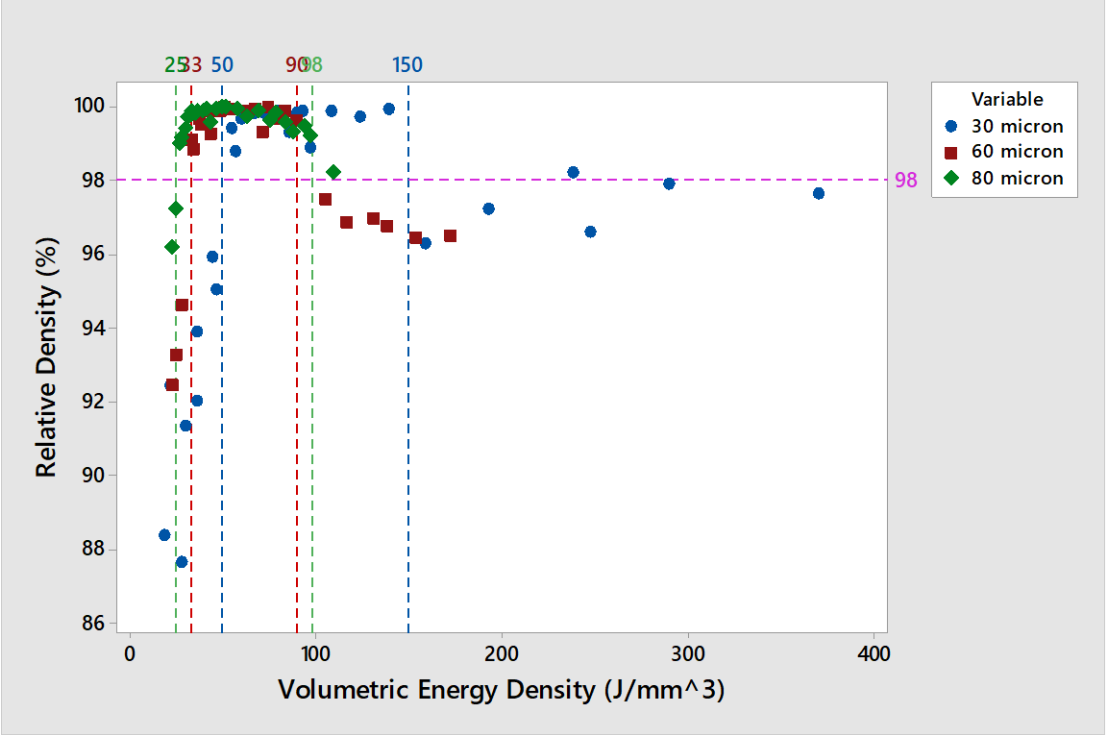

Figure 41: Comparison of results for increasing layer thickness

4.3 Selection of Optimum Process Parameters

All the process parameter development studies were done on a simple geometry of a 10 mm cube. As additive manufacturing is mainly used to manufacture complex geometries, in the practical applications geometry will differ that from a cube. Thus, the parameters that work for a simple geometry may not give similar results.

In laser powder bed fusion, the parts being manufactured are surrounded with powder used to print previous layer. This process also generates high amount of heat and the thermal flow from the part to powder is different than the thermal flow from the part

itself shown in figure 42 (Saunders, 2017). Different VED will result in different thermal interaction of laser and powder causing variation in the print quality. To avoid this variation a VED window is required. Thus, while selecting the parameters using this argument a sufficient process margin was left for getting similar densities for varying geometries.

For Selecting optimum process parameters for 30µm layer thickness out of the 27 parameters designed for the experiment, the argument of needing a process margin was used. As discussed in earlier chapters the optimum range of VED for 30µm layer thickness was found to be between 50 J/mm^3 to 150 J/mm^3.

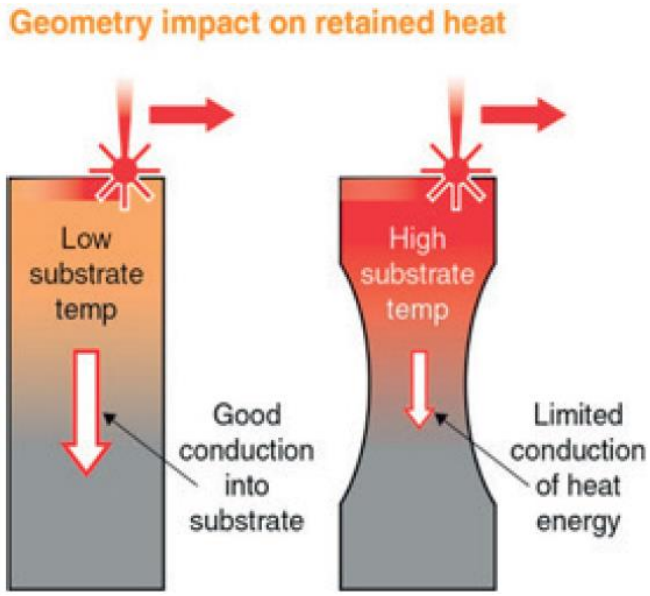

Figure 42: Geometry impact of heat (Saunders, 2017)

For Selecting optimum process parameters for 30µm layer thickness out of the 27 parameters designed for the experiment, the argument of needing a process margin was used. As discussed in earlier chapters the optimum range of VED for 30µm layer thickness was found to be between 50 J/mm^3 to 150 J/mm^3.

To check for variability in relative density due to build location 108 cube specimens were printed with 4 sets 27 cubes each. In figure 43 (a) it is seen that as the relative density increases standard deviation decreases. As for this study optimization of the parameters is to be done only for higher relative densities, the values were averaged. With this data of the average relative densities over the location for all the 27 parameters VED and relative densities were plotted as shown in figure 43 (b). Some of the specimens in this optimal window had unexpected surface properties. Some specimens had waviness to their surface while some had surface discoloration as shown in Figure 43 (c). Parameters for these specimens were eliminated for the final selection. With the specimens after the elimination a center value was selected amongst them. Selecting the center value will allow the VED to have a process margin. The selected VED for 30 μm layer thickness was 92.59 J/mm^3 and is shown in figure 43 (d). Final Optimized Process Parameters for this specimen are given in table 5.

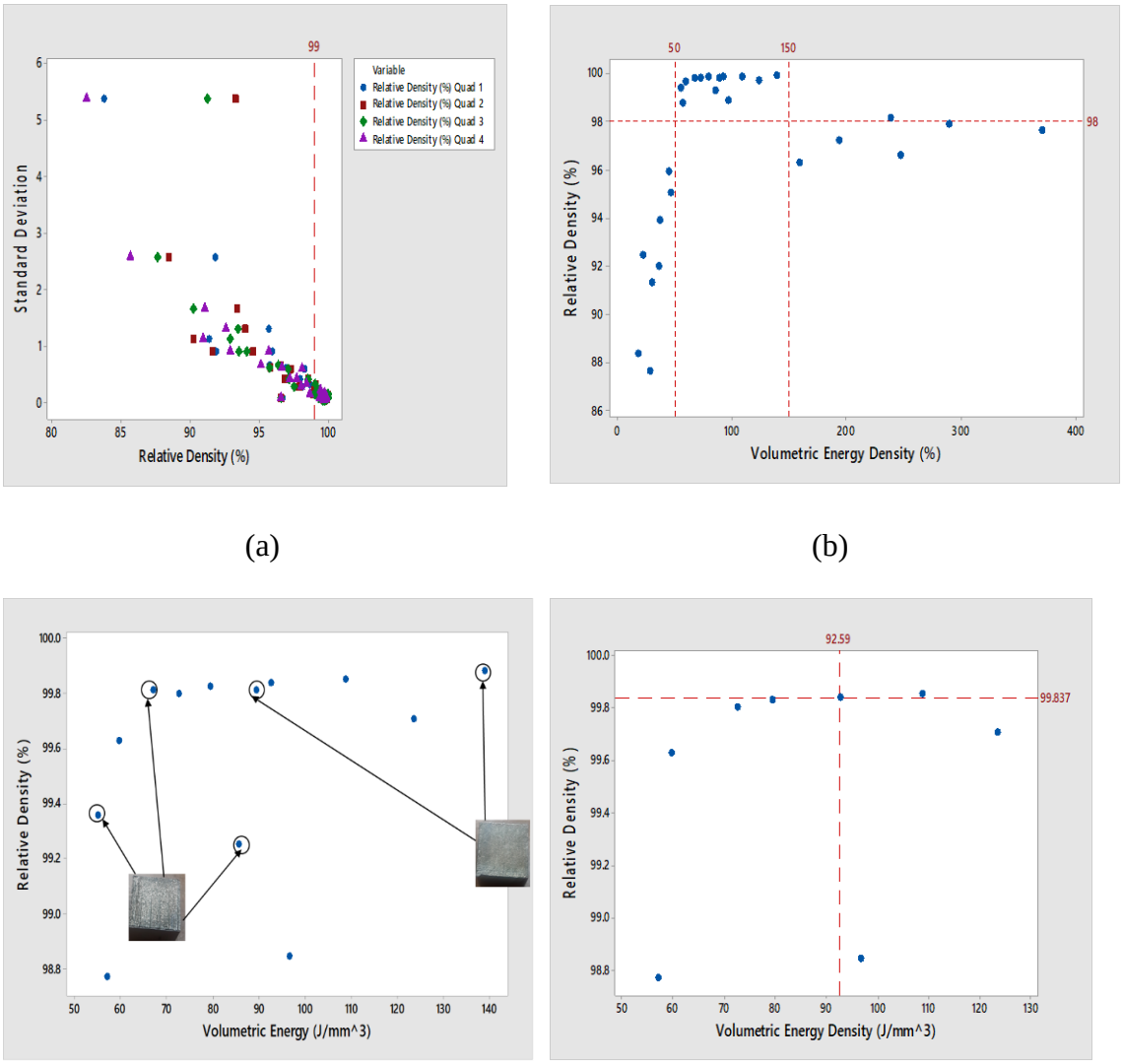

Figure 43: (a) Standard Deviation for Relative Density for 30 µm layer thickness (b) Average VED vs Relative density for 30 µm layer thickness (c) Elimination of Parameters for 30 µm layer thickness (d) Optimum VED for 30 µm layer thickness

With a similar approach for 60 µm layer thickness 108 of the DOE specimens, variability due to location was checked for these specimens. It was found that standard deviation decreases as the relative density increases. The standard deviation was negligible at higher densities as shown in Figure 44 (a). Therefore, the values for relative densities

were averaged and plotted against their corresponding VED as shown in Figure 44 (b). With the interest in high relative densities, specimens in the optimum window of VED for 60 μm layer thickness were inspected for any surface abnormalities. It was found that seven specimens closer to the lower bound of the VED window had surface abnormalities such as surface waviness, wrong form. Whereas five specimens closer to the higher bound of the VED window had surface discoloration. These eleven specimens were then eliminated. The center specimen of the remaining specimens was selected as the optimum for 60 μm layer thickness. This specimen had a VED of 56.19 J/mm^3 and the process parameters for this are in given in table 5

.

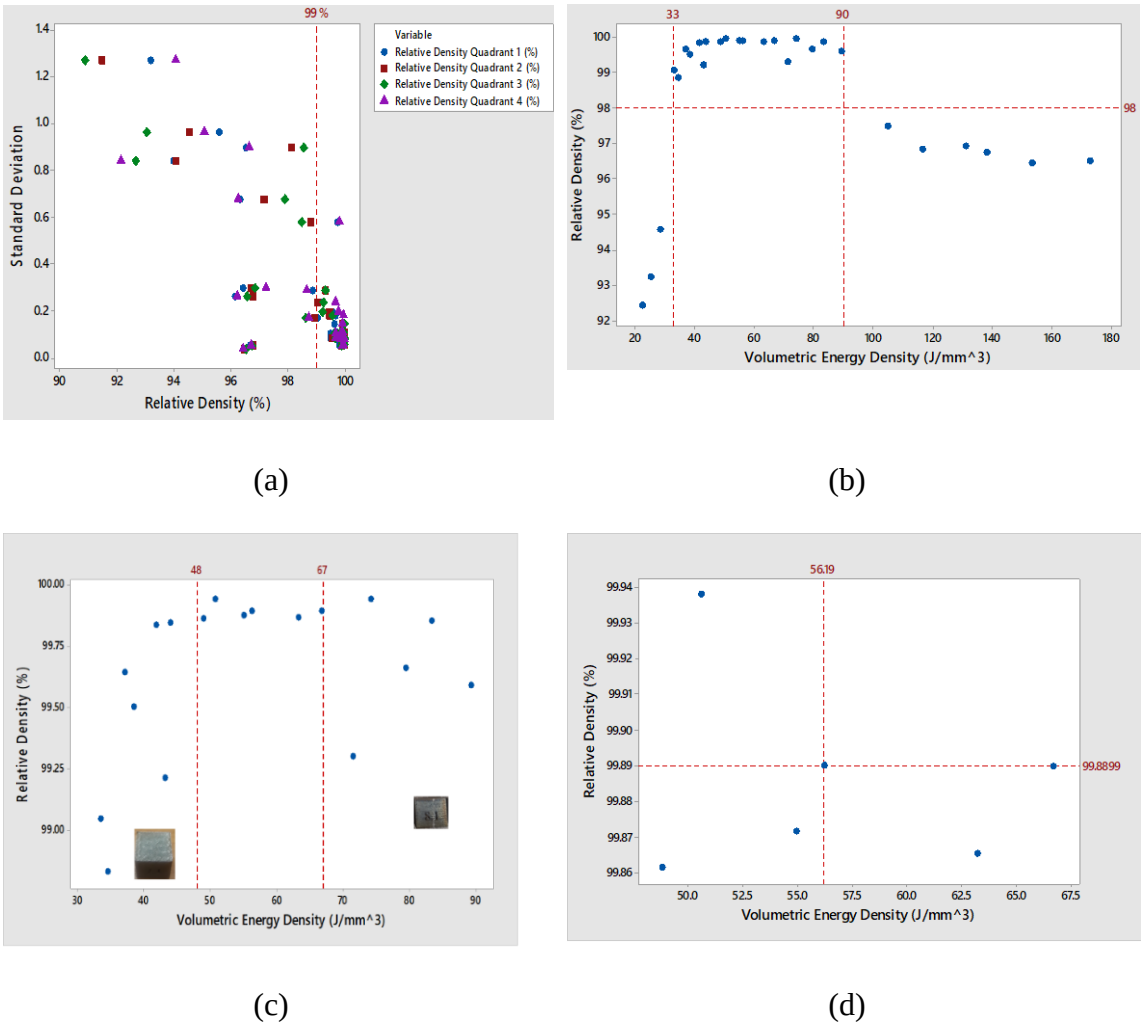

Figure 44: (a) Standard Deviation for Relative Density for 60µm layer thickness (b) Average VED vs Relative density for 60µm layer thickness (c) Elimination of Parameters for 60µm layer thickness (d) Optimum VED for 60µm layer thickness

Variance in relative density due to location for 80µm layer thickness final DOE specimens was checked. Figure 45 (a), shows that standard deviation decreases as the relative density increases. This trend of decreasing standard deviation was seen in specimen with lower layer thickness as well. As there was minimum standard deviation for specimens with relative density 99% and higher, the values for relative density were averaged. Figure 45 (b), shows the average relative density vs VED plot. Some of the

specimens with high densities in the optimal VED window were eliminated due to bad form and surface discoloration. The VED window was then further narrowed down to 39.4 J/mm^3 for lower bound and 63 J/mm^3 for the upper bound. A center value from these VED values were selected as the optimum VED for 80µm layer thickness. This specimen had a VED of 49.34 J/mm^3 and the process parameters in Table 5.

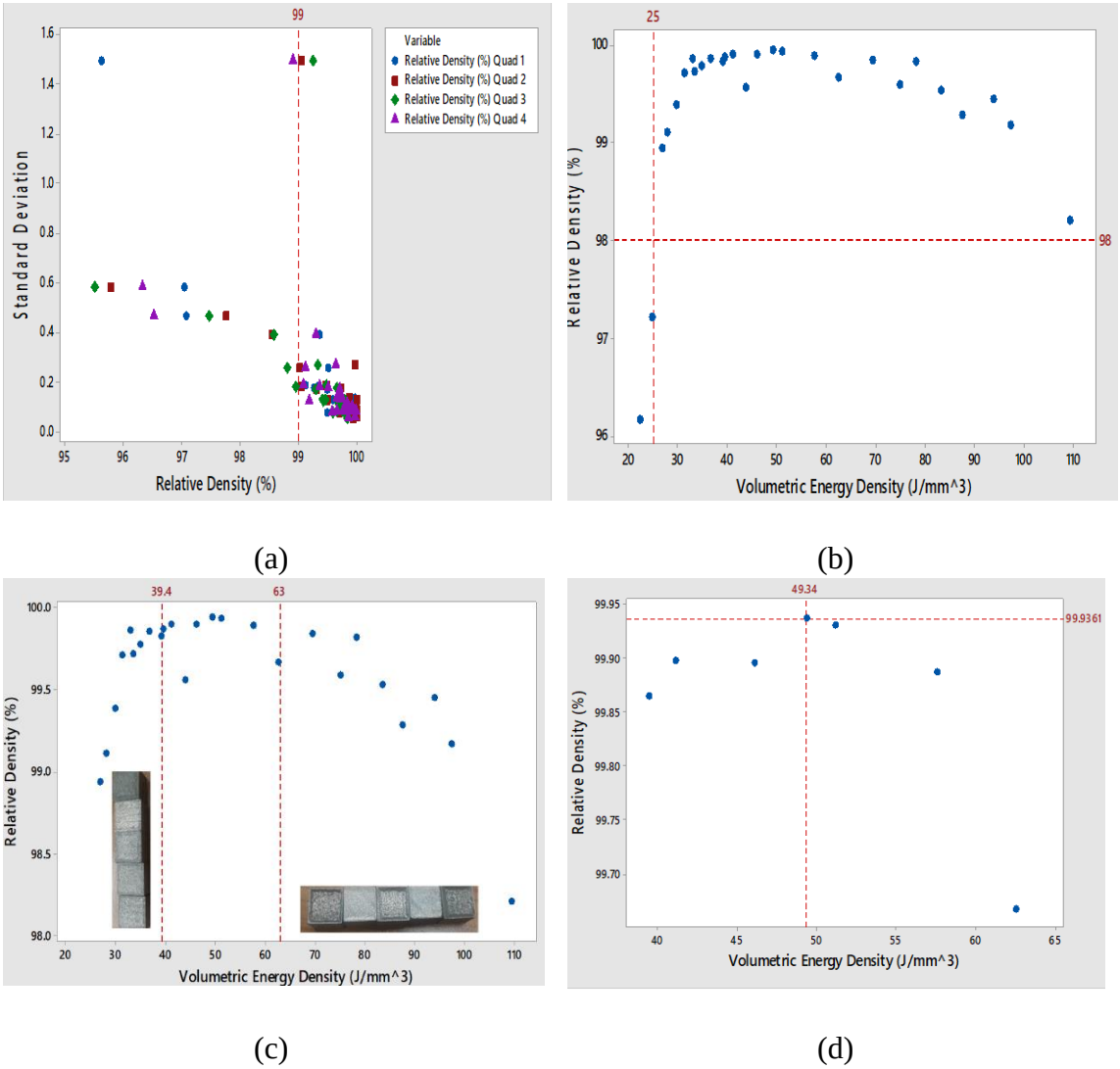

Figure 45: (a) Standard Deviation for Relative Density for 80 µm layer thickness (b) Average VED vs Relative density for 80 µm layer thickness (c) Elimination of Parameters for 80 µm layer thickness (d) Optimum VED for 80 µm layer thickness

Table 5 shows a summary of the final optimized parameters used to print tensile test coupons for property evaluation.

Layer Thickness (mm)	**Power (W)**	**Scan Velocity (mm/s)**	**Hatch Spacing (mm)**	**Volumetric Energy Density (J/mm^3)**
0.03	200	800	0.09	92.59
0.06	220	725	0.09	56.19
0.08	300	950	0.08	49.34

Table 5: Optimized Process Parameters

Testing of the dog-bones was conducted according to the method described in earlier chapters and was evaluated for Surface Roughness Relative Density and Mechanical Properties.

4.4 Mechanical Test Specimens

4.4.1 Surface roughness:

Surface roughness was evaluated for 300 dog bone specimens, 100 specimens of each 30μm, 60μm and 80μm layer thickness. To standardize the location on specimens, each measurement was taken on the vertical side face facing the operator. A horizontal line was marked with a pen 5 mm from the top edge of the specimen. The surface roughness was measured for a circular area of 19.687 mm^2 tangent to the horizontal line, so that the surface roughness is measure 5 mm below the horizontal line. Single image was taken with a high magnification and 40X zoom.

In Figure 46 (a), it is seen that there is a clear trend of increasing surface roughness with the increase of layer thickness. There was no significant effect due to the location of

specimen in X direction. Similarly in Figure 46 (b), it is seen that there is no effect of location. All the locations were measured from bottom right corner of the build plate in magics software. Physical measurements were not performed on the build plate.

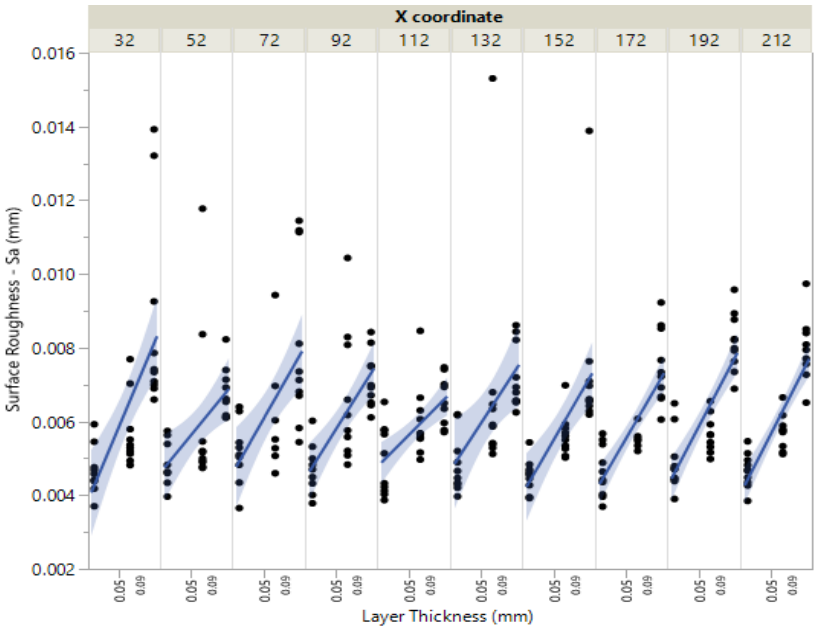

(a)

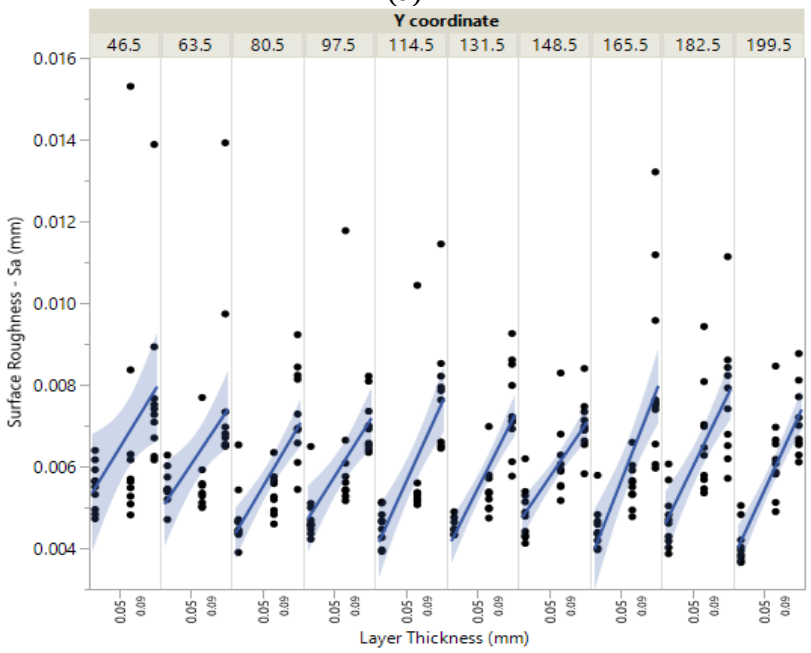

(b)

Figure 46: (a) Surface Roughness analysis over build location in X direction (b) Surface Roughness analysis over build location in Y direction

In figure 47, it is seen that the surface roughness increases with the increase in layer thickness and is statistically significant. The standard deviation is found to be increasing as well. The variances and means were not statistically equal. The mean surface roughness for 30µm layer thickness specimen was 0.0047799 mm, for 60µm was 0.0059747 mm and 0.0075488 mm for 80µm layer thickness.

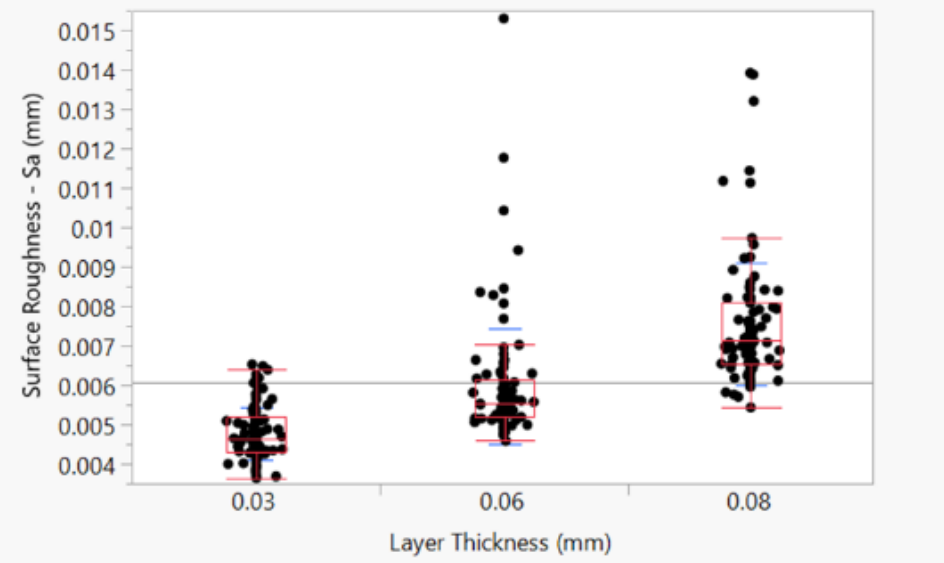

Tests that the Variances are Equal

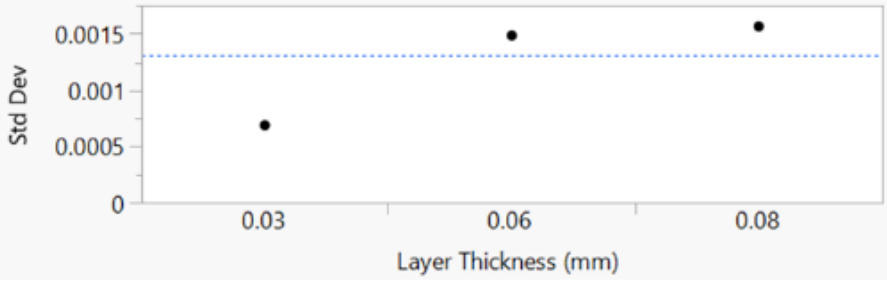

Means and Std Deviations

Level	Number	Mean	Std Dev	Std Err Mean	Lower 95%	Upper 95%
0.03	100	0.0047799	0.0006901	6.9012e-5	0.004643	0.0049169
0.06	100	0.0059747	0.0014866	0.0001487	0.0056797	0.0062696
0.08	99	0.0075488	0.0015672	0.0001575	0.0072362	0.0078614

Figure 47: Surface Roughness (S_a) vs Layer Thickness

4.4.2 Relative Density:

Relative Density was measured and analyzed for 300 dog bone specimens, 100 specimens of each 30 µm, 60 µm and 80 µm layer thickness. Specimens were measured by the method discussed in chapter 2.2

In figure 48, (a) and (b) it is seen that the relative density do not have a significant trend for changes in location. The values were plotted to see the change of relative density over changes in X coordinates and Y coordinates. All the measured values for all three layer thicknesses lie within the 100% range.

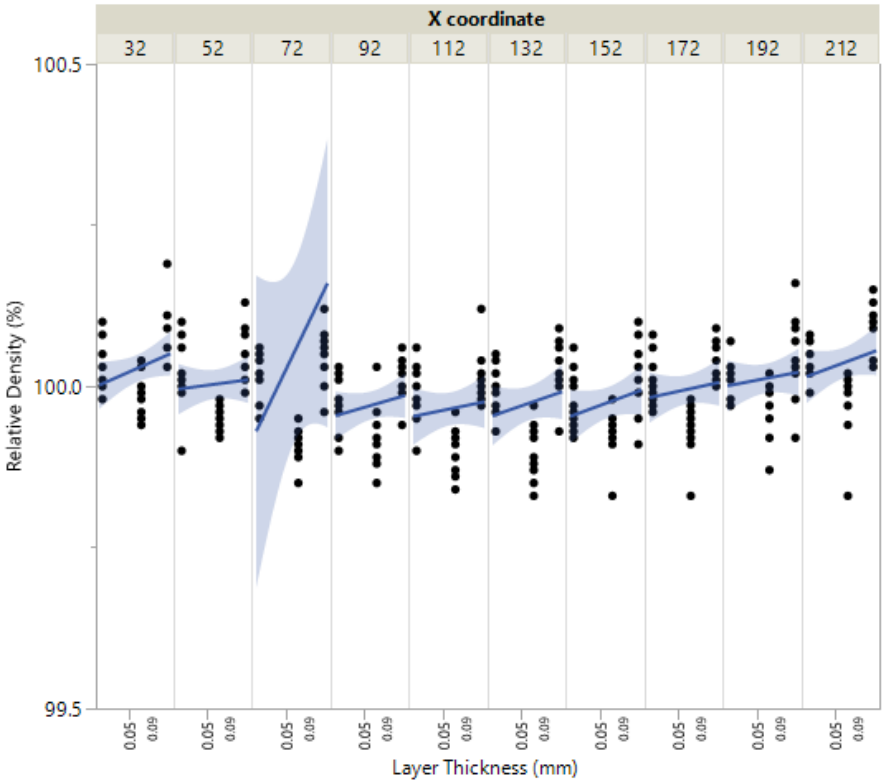

Figure 48 (a)

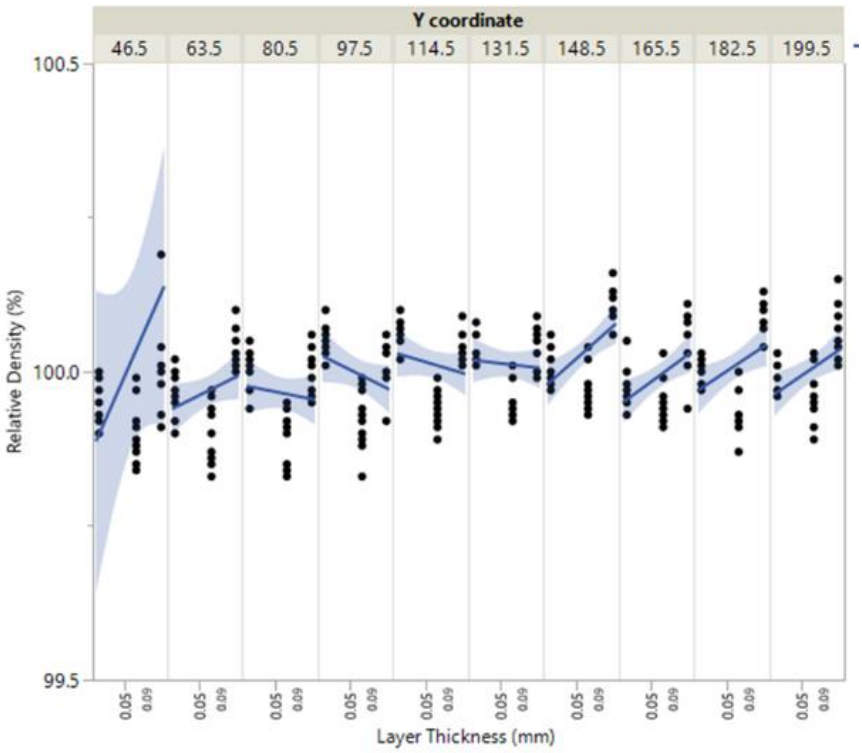

Figure 48 (b)

Figure 48: (a) Relative density analysis over build location in X direction (b) Relative density analysis over build location in Y direction

In Figure 49 it was observed that the relative densities had statistically significant differences in between the three layer thicknesses but means were within a 0.11% relative density range which suggests that they are technically equal. We can conclude that changes in layer thickness did not influence density.

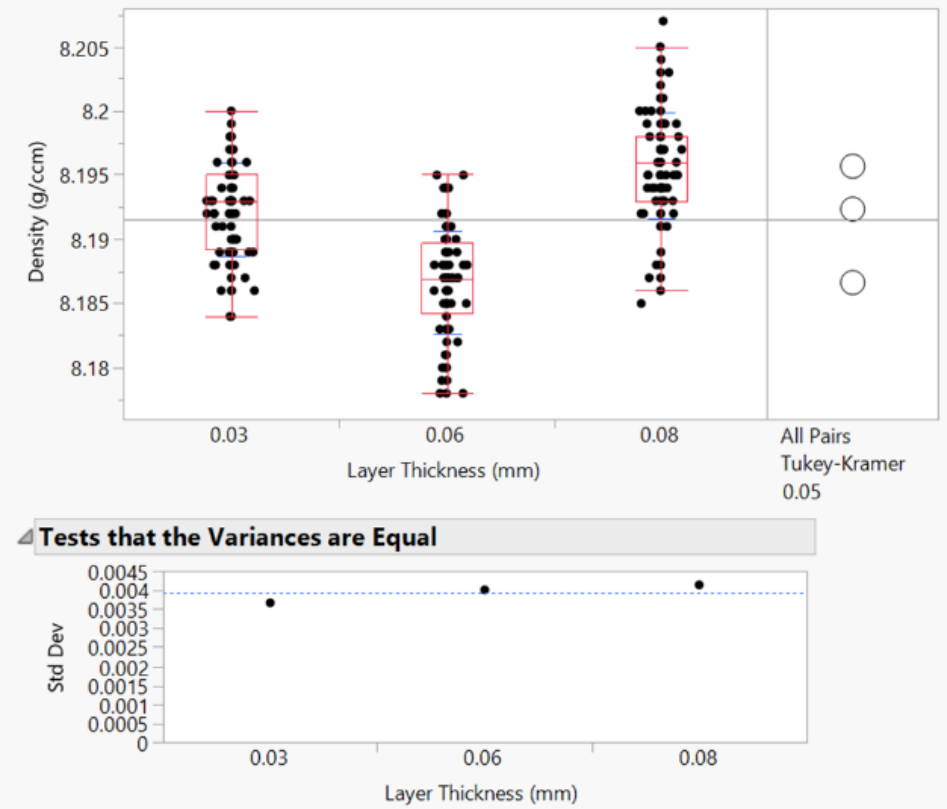

Connecting Letters Report

Level		Mean
0.08	A	100.04495
0.03	B	100.00430
0.06	C	99.93460

Levels not connected by same letter are significantly different.

Figure 49: Archimedes Density vs Layer Thickness

4.4.3 Mechanical Properties:

After testing the specimens for surface roughness and relative density, tensile tests were performed on these specimens. 30 specimens at each layer thickness were tested to analyze changes in Modulus, Yield Stress, True Ultimate Tensile Stress (UTS), Elongation and Necking as the layer thickness changes. Thickness of every specimen was measured using a micrometer and this value was used to analyze the data. All the tests were carried

out using the method discussed in Chapter 2.4. Importantly, these results are specimens that received no stress-relief, heat treatment, or Hot Isostatic Pressing (HIP), and as such represents a snapshot of what the behavior of these specimens is as-printed.

After measuring the specimen thickness by a micrometer, it was found that the thickness of the specimen increases with the increase in layer thickness. The nominal thickness of a specimen was 2mm, whereas the mean thickness was 2.005 mm at 30 µm, 2.049 mm for 60 µm and 2.0727 mm for 80 µm layer thickness. Figure 50 shows that there was no statistical equivalence for the specimen thickness at all the layer thicknesses.

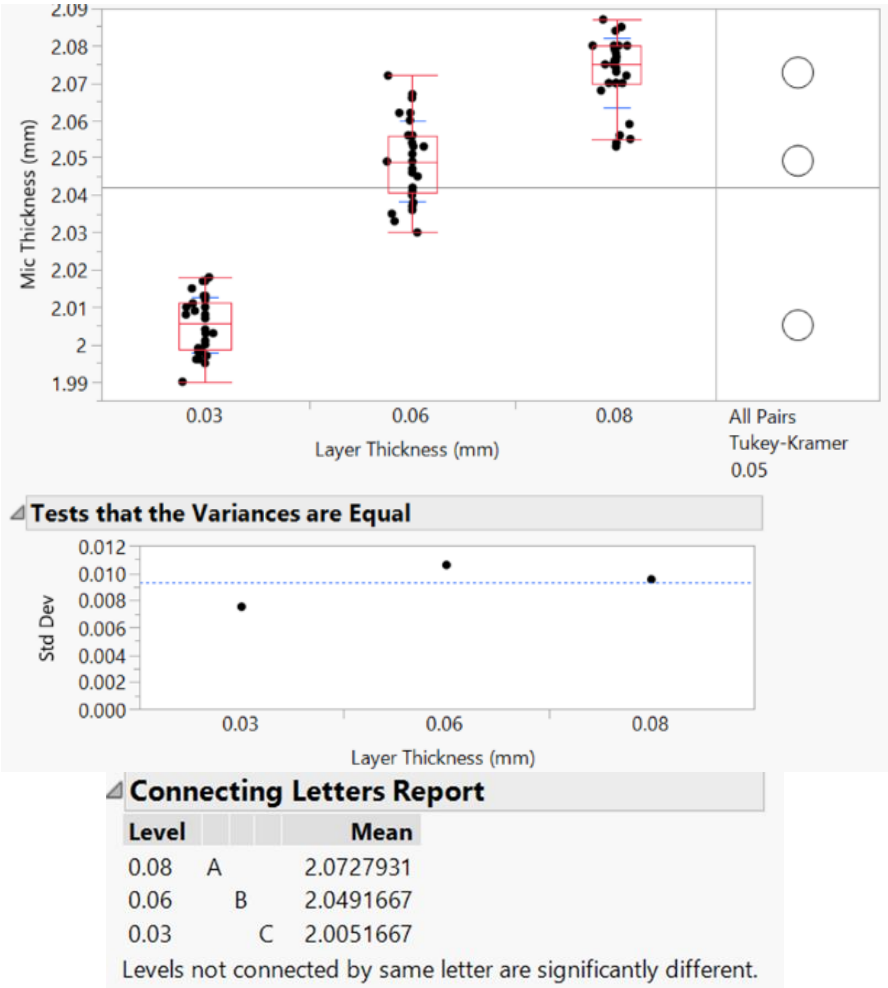

Figure 50: Specimen Thickness (Nominal = 2mm) vs Layer Thickness

Figure 51 shows the stress vs strain graph for all the 90 specimens with different layer thicknesses tested at a strain rate of 10^{-3}. Initial inference can be drawn that thir is significant drop in the yield with increase of layer thickness. The results were consistent for all specimens with a layer thickness.

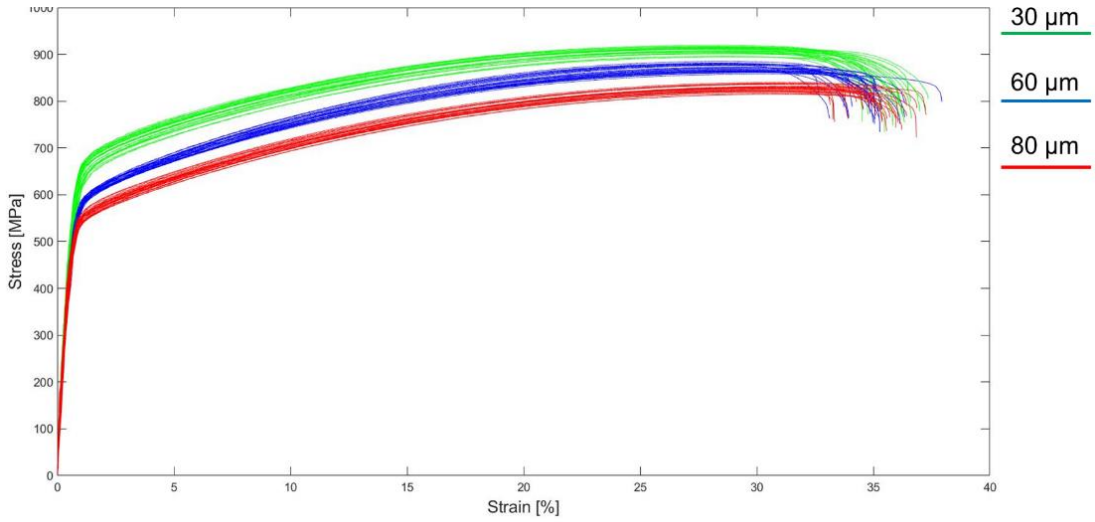

Figure 51: Stress (Mpa) vs Strain (%) Graph (30 specimens of each layer thickness)

Modulus:

It was observed that there was no significant effect on the modulus as the layer thickness increases. Figure 52, shows that for Modulus, means and sigmas are statistically equivalent for all 3 layer thicknesses. The obtained mean modulus was 90.044 Gpa for 30 µm, 82 Gpa for 60 µm, and 81.67 Gpa for 80 µm layer thickness.

Figure 52 shows that for Modulus, means and sigmas are statistically equivalent for all 3 layer thicknesses.

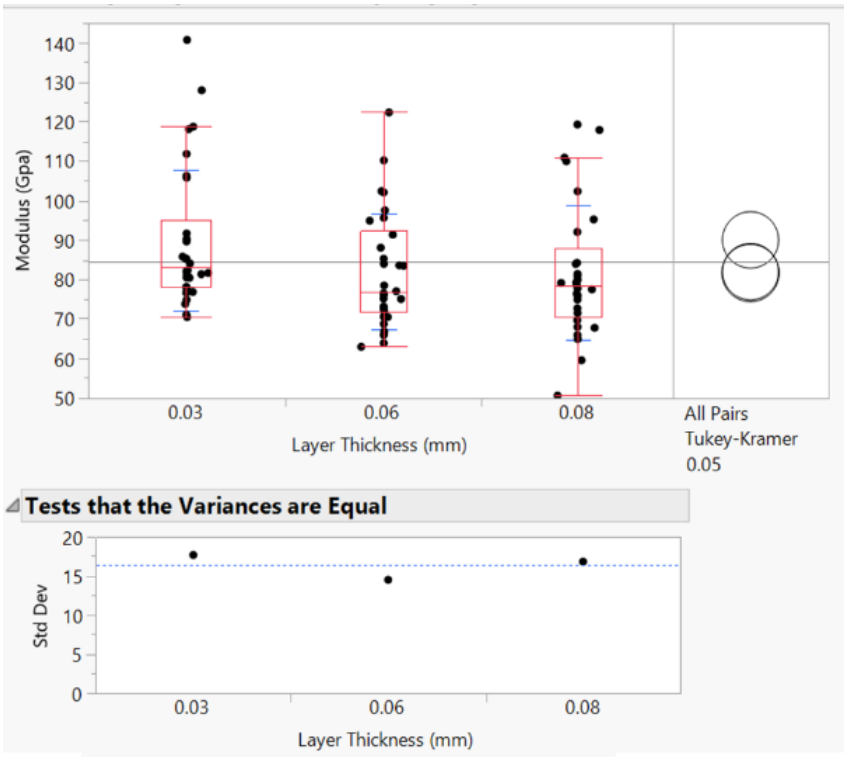

Tests that the Variances are Equal

Connecting Letters Report

Level		Mean
0.03	A	90.044540
0.06	A	82.001333
0.08	A	81.670690

Levels not connected by same letter are significantly different.

Figure 52: Modulus vs Layer Thickness

Yield Stress:

Yield stress is observed to decrease significantly with an increase in layer thickness. It was observed that mean yield stress was 600.10 Mpa for 30 µm, 525.18 Mpa for 60 µm and 504.78 Mpa for 80 µm layer thickness. From Figure 53, it can be inferred that no statistical equivalence was observed with the change in layer thickness.

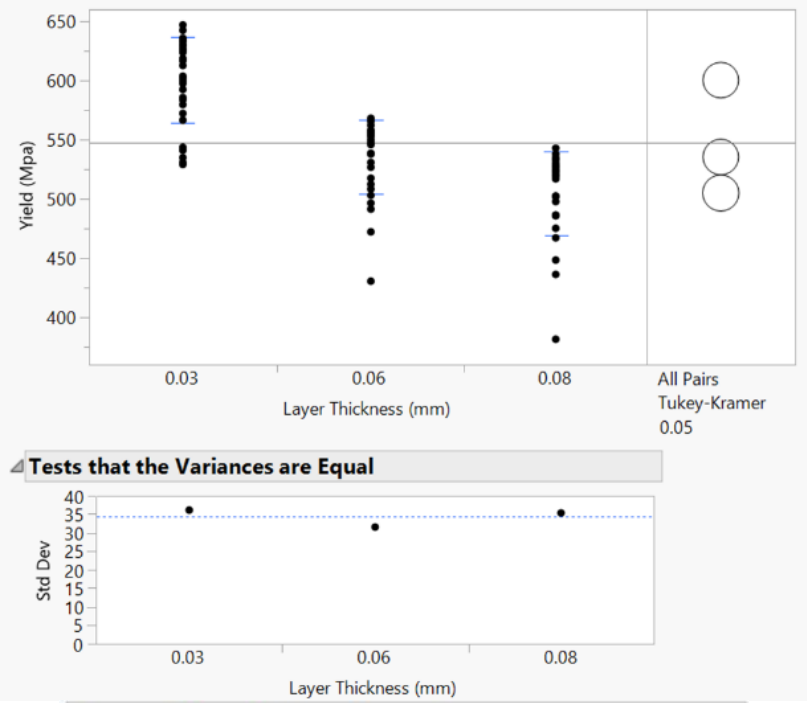

Tests that the Variances are Equal

Connecting Letters Report

Level		Mean
0.03	A	600.10100
0.06	B	535.17967
0.08	C	504.78655

Levels not connected by same letter are significantly different.

Figure 53: Yield Stress vs Layer Thickness

True Ultimate Tensile Stress:

From Figure 54, It is observed that the True UTS drops significantly with the increase in layer thickness.

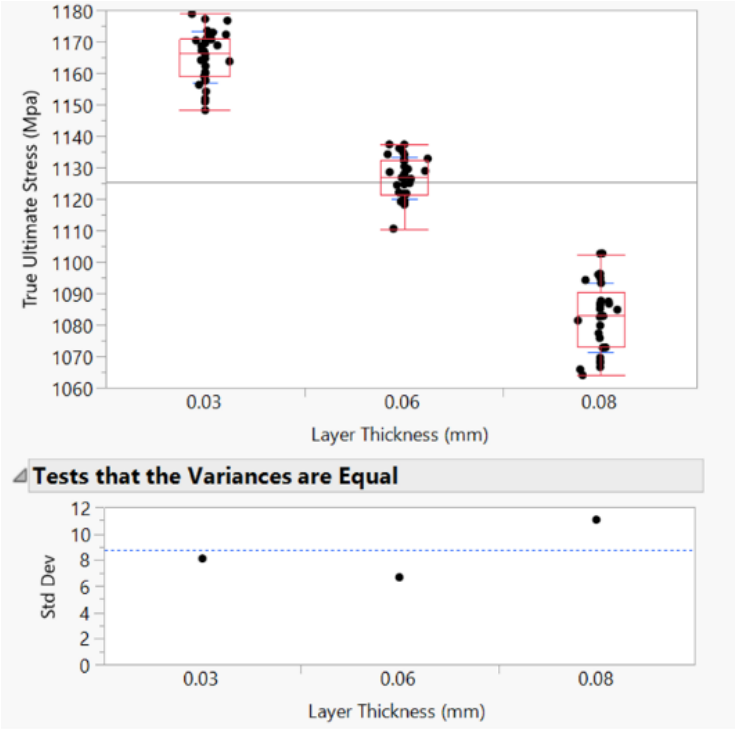

Figure 54: True UTS vs Layer Thickness

The effects of location on UTS were tested for all 3 layer thickness. It was observed from Figure 55 that for 30 and 80 µm layer thickness higher UTS is observed in between 75 mm and 150 mm in the X- direction. No significant trends for 60 µm layer thickness. There were no trends observed in Y-direction.

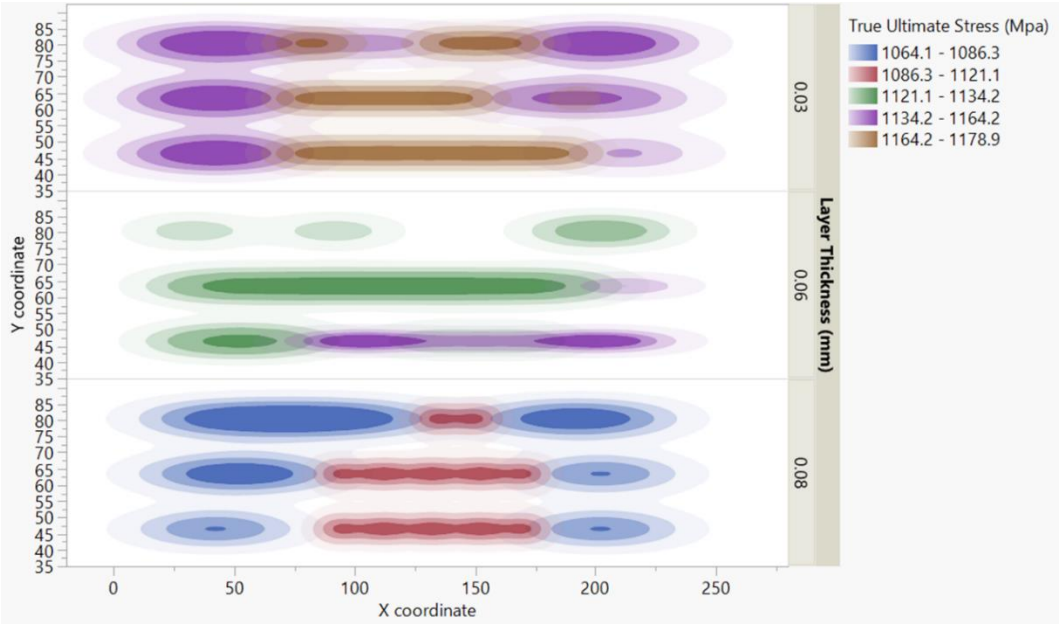

Figure 55: UTS variability across build plate

Elongation:

For elongation of the specimens it was seen from Figure 56, that there was a statistical difference between 30µm and 60µm layer thickness but as the difference was approximately 1%, it technically cannot be a significant difference.

The mean Elongation from Figure 50 was 35.75% for 30 µm, 34.93% for 60 µm and 35.22% for 80µm layer thickness.

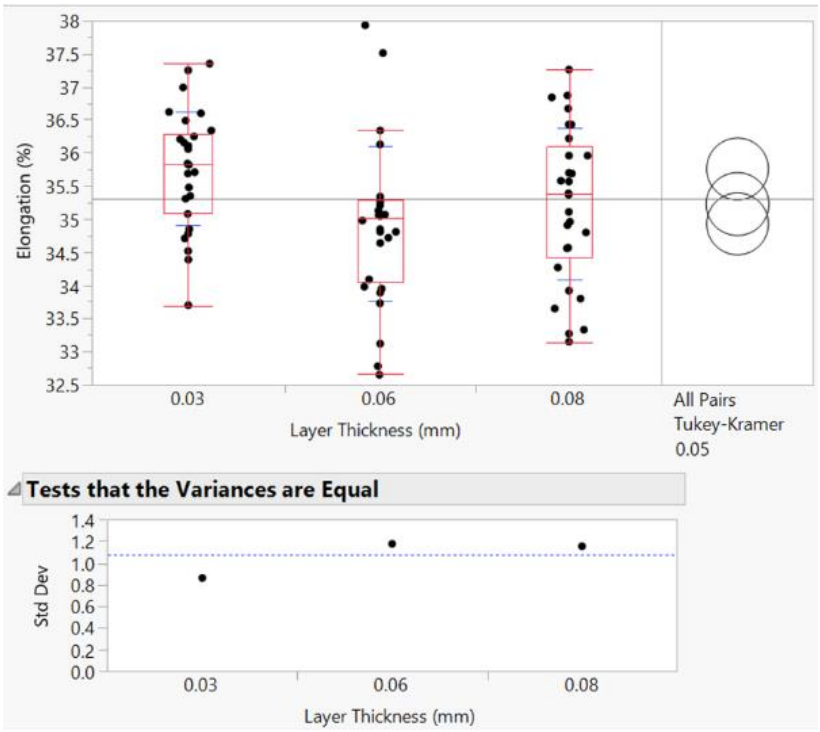

Tests that the Variances are Equal

Test	F Ratio	DFNum	DFDen	Prob > F
O'Brien[.5]	1.2993	2	86	0.2780
Brown-Forsythe	0.9796	2	86	0.3796

Connecting Letters Report

Level			Mean
0.03	A		35.759333
0.08	A	B	35.228276
0.06		B	34.929667

Figure 56: % Elongation vs Layer Thickness

Necking:

Necking in the specimens reduced with the increase in the layer thickness. There were statistically significant differences in the 3 layer thicknesses. From Figure 51, Mean Necking was 7.52% for 30 µm, 5.63% for 60 µm and 4.24% for 80 µm

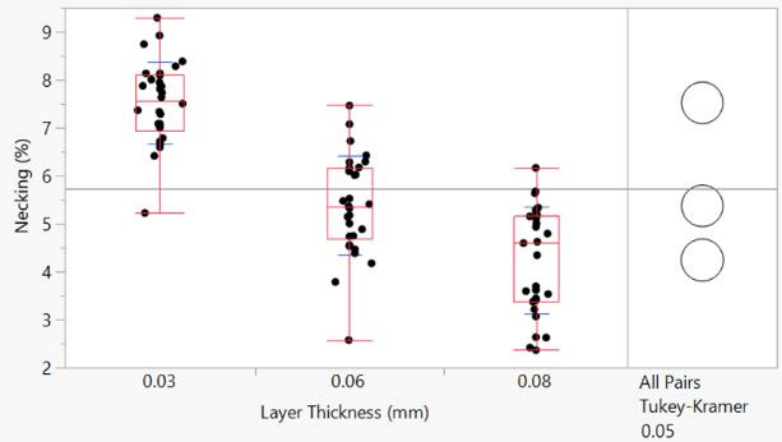

Tests that the Variances are Equal

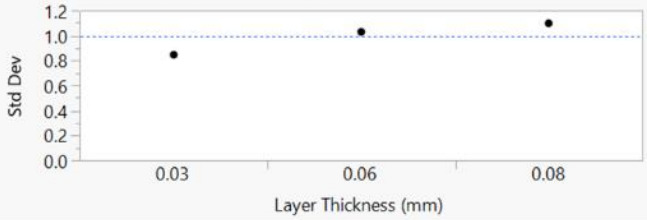

Test	F Ratio	DFNum	DFDen	Prob > F
O'Brien[.5]	1.0268	2	86	0.3625
Brown-Forsythe	1.7559	2	86	0.1789

Connecting Letters Report

Level				Mean
0.03	A			7.5170000
0.06		B		5.3676667
0.08			C	4.2375862

Levels not connected by same letter are significantly different.

Figure 57: % Necking vs Layer Thickness

CHAPTER 5

DISCUSSION AND FUTURE WORK

This thesis reported how surface and mechanical properties change as a function of layer thickness, in as-printed Inconel 718 manufactured with the Laser Powder Bed Fusion (LPBF) process. Optimizing parameters at each layer thickness demonstrated feasibility of obtaining greater than 99% relative density in these parts, with no significant differences across layer thicknesses. On the other hand, debits were seen in as-printed surface roughness and strength properties, which will need further study prior to production implementation. However, this work shows the feasibility of printing at higher thicknesses. In this final chapter, a few additional points are discussed, followed by a summary of recommendations for future work.

5.1 Soot generation

The generation of soot was found to increase with the increase in layer thickness, seen in Figure 58. The initial gas flow was to overcome this problem ventilator speed was increased to 100%-90% it was observed that all the powder was carried away with the gas. The gas flow was further reduced to 70% and it was observed that not all but most of the powder was carried away with the gas.

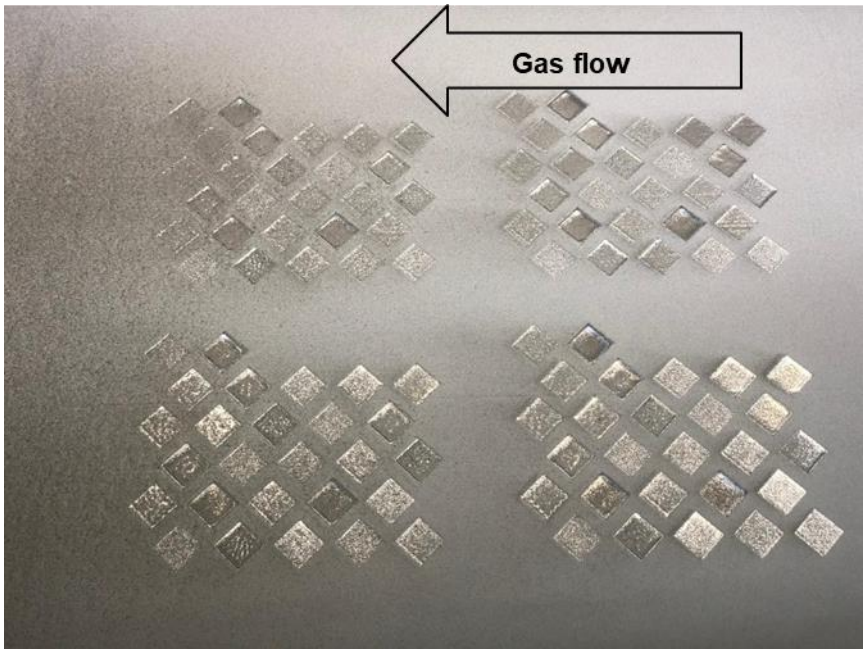

Figure 58: Soot Deposited on powder bed (left side)

The gas flow was then reduced to 65% and the powder was moving from one location to other on the build plate in direction of gas flow. This caused the powder bed to become uneven. Thus, 60% ventilator speed was used to print the specimens.

While this change in gas flow was being performed, the print failed with part and coater blade interaction which can be seen in Figure 59. This phenomenon is associated with the ventilator design. A change in ventilator design can increase in the soot carrying efficiency.

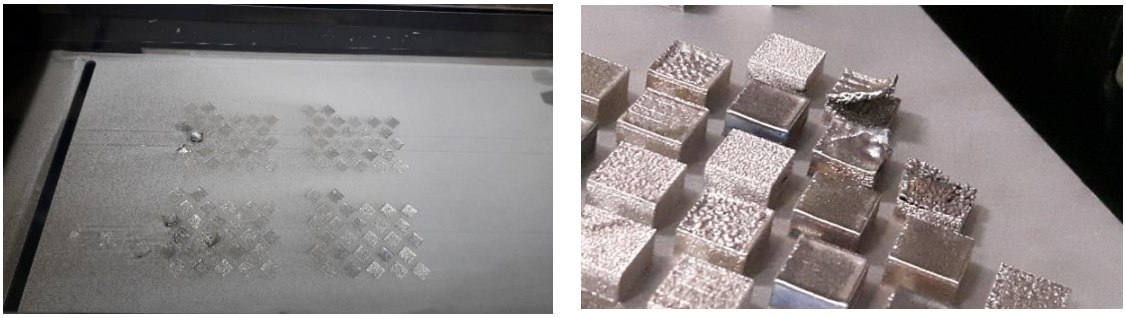

(a) (b)

Figure 59: (a) Powder Starvation (b) Failed Build

5.2 Towards a Time Model

A high-level preliminary time model was created to evaluate the time difference in the change of layer thickness and velocity. The following equations was build considering a geometry of a cube.

Volume of a cube can be taken as the height times the cross-sectional area. For scanning time for one pass of the laser over the cube will be the length of the cube. With the known velocity time taken to travel this distance can be calculated. For an area the same distance will be traveled multiple times. To calculate this, breadth of the cube can be divided by hatch distance to get the number of passes to cover the whole area. Multiplying these two will give the time to scan the cross-sectional area. The height of the cube was divided by the layer thickness to get the number of layers when these number of layers are multiplied with the time for one cross-sectional area will give the scanning time for the whole cube. When the denominators and numerators were simplified it was observed that the volume of the cube when divided by the product of velocity, hatch distance and layer thickness gave the scanning time. For coating time, time was calculated using a stop watch

for coating of one layer. The stop watch was started when laser scanning was stopped and was stopped when the laser scanning started again. In this activity time taken by the coater blade to coat one layer was calculated. For the whole cube it was then multiplied with the total numbers and then added to the scanning time to get the total time.

$$T = t1 + t2$$

$$t1 = \frac{H}{l} * \mathrm{C}$$

$$t2 = \frac{V}{v * t * h}$$

Where: T : Total Time (s), $t1$: Coating Time (s), $t2$: Scanning Time (s), H : Height of Specimen (mm), V : Volume of one layer (mm^3), v : Scan Velocity (mm/s), t : Layer thickness (mm), h : Hatch Distance (mm), l : Layer Thickness (mm), C : Coating time for one layer (s)

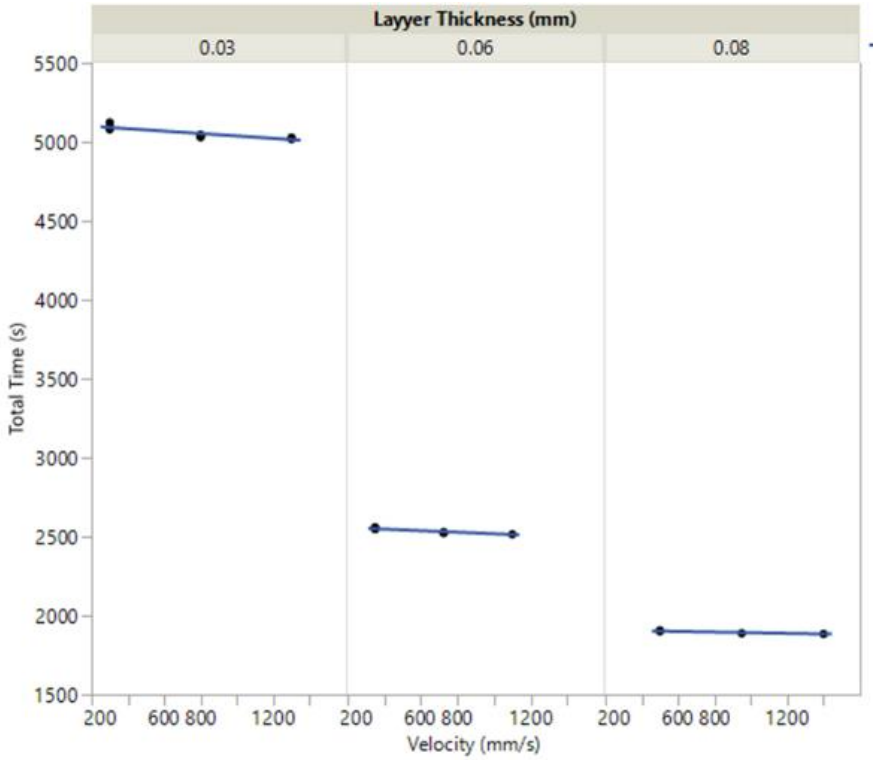

Figure 60: Layer Thickness (mm) vs Total Time (s)

As It is seen layer thickness has a prominent effect on time a theory of increase of layer thickness to a higher value was evaluated. It was assumed that the velocity for these specimens dropped in steps of 50 mm/s from a maximum of 1400 mm/s and a constant hatch distance of 0.08 mm was selected. After calculating the time for further increase in layer thicknesses. It was seen that the significance in time reduction dropped after 150µm microns layer thickness. This effect can be seen in figure 61.

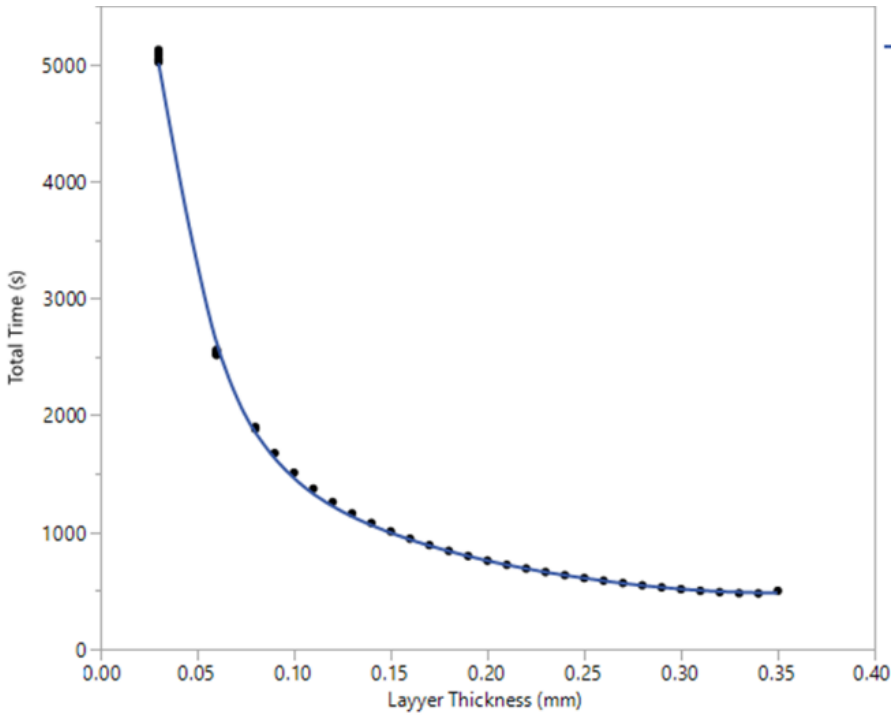

Figure 61: Total Time vs Layer Thickness

5.3 Future Work

It was observed that increasing layer thickness can result in significant changes in properties, like surface roughness. As none of the parameters were optimized for surface roughness, optimizing parameters for surface roughness and then evaluating the changes in properties can be evaluated.

Mechanical properties showed that properties like UTS reduces significantly with increase in layer thickness. As none of the specimens under went any heat treatment, while many industrial applications require heat treatment of the specimens. Effects of heat treatments to compare the properties with as build specimens can be done. Also evaluating micro structure of these specimens can give insights of the change in properties.

REFERENCES

Alafaghani, A., Qattawi, A., & Castañón, M. A. G. (2018). Effect of manufacturing parameters on the microstructure and mechanical properties of metal laser sintering parts of precipitate hardenable metals. *International Journal of Advanced Manufacturing Technology*, *99*(9–12), 2491–2507. https://doi.org/10.1007/s00170-018-2586-5

Amato, K. N., Gaytan, S. M., Murr, L. E., Martinez, E., Shindo, P. W., Hernandez, J., … Medina, F. (2012). Microstructures and mechanical behavior of Inconel 718 fabricated by selective laser melting. *Acta Materialia*, *60*(5), 2229–2239. https://doi.org/10.1016/j.actamat.2011.12.032

ASTM E8. (2010). ASTM E8/E8M standard test methods for tension testing of metallic materials 1. *Annual Book of ASTM Standards 4*. https://doi.org/10.1520/E0008

ASTM International. (2013). *F2792-12a - Standard Terminology for Additive Manufacturing Technologies*. *Rapid Manufacturing Association*. https://doi.org/10.1520/F2792-12A.2

Brown, C. U., Jacob, G., Possolo, A., Beauchamp, C., Peltz, M., Stoudt, M., & Donmez, A. (2018). The effects of laser powder bed fusion process parameters on material hardness and density for nickel alloy 625. *NIST Advanced Manufacturing Series*, 100–119. https://doi.org/10.6028/NIST.AMS.100-19

Caiazzo, F., Alfieri, V., Corrado, G., & Argenio, P. (2017). Laser powder-bed fusion of Inconel 718 to manufacture turbine blades. *International Journal of Advanced Manufacturing Technology*, *93*(9–12), 4023–4031. https://doi.org/10.1007/s00170-017-0839-3

Choi, J. P., Shin, G. H., Yang, S., Yang, D. Y., Lee, J. S., Brochu, M., & Yu, J. H. (2017). Densification and microstructural investigation of Inconel 718 parts fabricated by selective laser melting. *Powder Technology*. https://doi.org/10.1016/j.powtec.2017.01.030

Jia, Q., & Gu, D. (2014a). Selective laser melting additive manufactured Inconel 718 superalloy parts: High-temperature oxidation property and its mechanisms. *Optics and Laser Technology*, *62*, 161–171. https://doi.org/10.1016/j.optlastec.2014.03.008

Jia, Q., & Gu, D. (2014b). Selective laser melting additive manufacturing of Inconel 718 superalloy parts: Densification, microstructure and properties. *Journal of Alloys and Compounds*, *585*, 713–721. https://doi.org/10.1016/j.jallcom.2013.09.171

Jr, P. F. K. (2016). Fatigue Behavior of Direct Metal Laser Sintered A thesis submitted by, (February).

Karimi, P., Raza, T., Andersson, J., & Svensson, L. E. (2018). Influence of laser exposure time and point distance on 75-μm-thick layer of selective laser melted Alloy 718. *International Journal of Advanced Manufacturing Technology*. https://doi.org/10.1007/s00170-017-1019-1

Kuo, Y. L., Horikawa, S., & Kakehi, K. (2017). Effects of build direction and heat treatment on creep properties of Ni-base superalloy built up by additive manufacturing. *Scripta Materialia*, *129*, 74–78. https://doi.org/10.1016/j.scriptamat.2016.10.035

Ladewig, A., Schlick, G., Fisser, M., Schulze, V., & Glatzel, U. (2016). Influence of the shielding gas flow on the removal of process by-products in the selective laser melting process. *Additive Manufacturing*. https://doi.org/10.1016/j.addma.2016.01.004

Lindemann, C., Jahnke, U., Moi, M., & Koch, R. (2012). Analyzing product lifecycle costs for a better understanding of cost drivers in additive manufacturing. In *23rd Annual International Solid Freeform Fabrication Symposium - An Additive Manufacturing Conference, SFF 2012*.

Popovich, V. A., Borisov, E. V., Popovich, A. A., Sufiiarov, V. S., Masaylo, D. V., & Alzina, L. (2017). Functionally graded Inconel 718 processed by additive manufacturing: Crystallographic texture, anisotropy of microstructure and mechanical properties. *Materials and Design*, *114*, 441–449. https://doi.org/10.1016/j.matdes.2016.10.075

Read, N., Wang, W., Essa, K., & Attallah, M. M. (2015). Selective laser melting of AlSi10Mg alloy: Process optimisation and mechanical properties development. *Materials and Design*. https://doi.org/10.1016/j.matdes.2014.09.044

Rickenbacher, L., Spierings, A., & Wegener, K. (2013). An integrated cost-model for selective laser melting (SLM). *Rapid Prototyping Journal*. https://doi.org/10.1108/13552541311312201

Sadowski, M., Ladani, L., Brindley, W., & Romano, J. (2016). Optimizing quality of additively manufactured Inconel 718 using powder bed laser melting process. *Additive Manufacturing*, *11*, 60–70. https://doi.org/10.1016/j.addma.2016.03.006

Saunders, M. (2017). X marks the spot - find ideal process parameters for your metal AM parts, *44*(0), 1–13.

Sochalski-Kolbus, L. M., Payzant, E. A., Cornwell, P. A., Watkins, T. R., Babu, S. S., Dehoff, R. R., … Duty, C. (2015). Comparison of Residual Stresses in Inconel 718 Simple Parts Made by Electron Beam Melting and Direct Laser Metal Sintering. *Metallurgical and Materials Transactions A: Physical Metallurgy and Materials Science*, *46*(3), 1419–1432. https://doi.org/10.1007/s11661-014-2722-2

Sufiiarov, V. S., Borisov, E. V., & Polozov, I. A. (2014). Selective Laser Melting of the Inconel 718 Nickel Superalloy. *Applied Mechanics and Materials*, *698*, 333–338. https://doi.org/10.4028/www.scientific.net/amm.698.333

Tillmann, W., Schaak, C., Nellesen, J., Schaper, M., Aydinöz, M. E., & Hoyer, K. P. (2017). Hot isostatic pressing of IN718 components manufactured by selective laser melting. *Additive Manufacturing*, *13*, 93–102. https://doi.org/10.1016/j.addma.2016.11.006

Wang, Z., Guan, K., Gao, M., Li, X., Chen, X., & Zeng, X. (2012). The microstructure and mechanical properties of deposited-IN718 by selective laser melting. *Journal of Alloys and Compounds*, *513*, 518–523. https://doi.org/10.1016/j.jallcom.2011.10.107

Xia, M., Gu, D., Yu, G., Dai, D., Chen, H., & Shi, Q. (2016). Influence of hatch spacing on heat and mass transfer, thermodynamics and laser processability during additive manufacturing of Inconel 718 alloy. *International Journal of Machine Tools and Manufacture*, *109*, 147–157. https://doi.org/10.1016/j.ijmachtools.2016.07.010